Antifungal activity of Co(II) and Cu(II) complexes containing 1,3-bis(benzotriazol-1-yl)-propan-2-ol on the growth and virulence traits of fluconazole-resistant *Candida* species: synthesis, DFT calculations, and biological activity

Ricardo A. Murcia-Galán[1], Sandra M. Durán[2], Sandra M. Leal-Pinto[2], Martha V. Roa-Cordero[2], Jose D. Vargas[2], Laura V. Herrera[3], Alvaro Muñoz-Castro[4], Desmond MacLeod-Carey[5], Tonny W. Naranjo[6,7], Peter L. Rodríguez-Kessler[8] and John J. Hurtado[1]*

Abstract

Relevant virulence traits in *Candida* spp. are associated with dimorphic change and biofilm formation, which became an important target to reduce antifungal resistance. In this work, Co(II) complexes containing a benzotriazole derivative ligand showed a promising capacity of reducing these virulence traits. These complexes exhibited higher antifungal activities than the free ligands against all the *Candida albicans* and non-*albicans* strains tested, where compounds **2** and **4** showed minimum inhibitory concentration values between 15.62 and 125 µg mL^{-1}. Moreover, four complexes (**2–5**) of Co(II) and Cu(II) with benzotriazole ligand were synthesized. These compounds were obtained as air-stable solids and characterized by melting point, thermogravimetric analysis, infrared, Raman and ultraviolet/visible spectroscopy. The analysis of the characterization data allowed us to identify that all the complexes had 1:1 (M:L) stoichiometries. Additionally, Density Functional Theory calculations were carried out for **2** and **3** to propose a probable geometry of both compounds. The conformer **Da** of **2** was the most stable conformer according to the Energy Decomposition Analysis; while the conformers of **3** have a fluxional behavior in this analysis that did not allow us to determine the most probable conformer. These results provide an important platform for the design of new compounds with antifungal activities and the capacity to attack other target of relevance to reduce antimicrobial resistance.

Keywords Benzotriazole ligand, Cobalt(II) and copper(II) complexes, Antifungal activity, Antibiofilm agents, *Candida* species, Virulence traits

*Correspondence:
John J. Hurtado
jj.hurtado@uniandes.edu.co
Full list of author information is available at the end of the article

Murcia-Galán *et al. BMC Chemistry*   (2023) 17:135

Page 2 of 21

Introduction

Antimicrobial resistance (AMR) occurs when bacteria, fungi, viruses, or parasites change over time and no longer respond to medicines used to treat infections, making them harder to treat, increasing the risk of disease spread, severe illness, and death. AMR is a primary concern for public health threats since a considerable number of strains of different pathogenic microorganisms with AMR are emerging, which has increased the morbidity and mortality rates of humans and animals due to infectious diseases [1, 2]. During 2019, nearly 4.95 million human deaths were associated with bacterial AMR, including 1.27 million deaths directly attributable to bacterial AMR [3].

This increase in AMR has occurred due to excessive and inappropriate use of antimicrobials and the transfer of resistant genes between homologous strains present in different environments (farm animals and the environment) [4, 5]. Moreover, infectious diseases of resistant strains primarily put at risk people undergoing surgical procedures, organ transplants, immunosuppressive procedures (such as chemotherapy), and the care of newborns [1, 6–11]. Among the resistant microorganisms, *Candida* strains stand out, of which several mechanisms linked to their resistance are already known: overexpression or mutation of the target enzyme, concordances of the biosynthetic pathway of the target compound, formation of biofilms, changes in the permeability of the cell membrane, among others [12–15]. The ability of *Candida* species to form biofilms makes it an important pathogen of infections associated with health care, and its presence on the surfaces of medical devices such as catheters is dependent on the ability of each species to produce extracellular polymeric substances (EPS) that contribute to the persistence of the microorganism [16]. Invasion and maintenance of biofilm architecture are further related to the ability of *Candida* to undergo a dimorphic change from yeast to hyphae, another important virulence trait [17]. For the above, the treatment of candidemia is a clinical challenge that demands the development of a new drug formulation with effects on virulence traits related to antifungal resistance. Thus, the inhibition of biofilm formation is an approach currently explored for developing antimicrobials that are more effective.

Compounds derived from azoles have been widely implemented against different strains of fungi due to their effectiveness and mechanism of action, which involves the inhibition of ergosterol synthesis that stops the growth and replication of the fungus [18, 19]. However, these azole compounds have decreased their antifungal activity due to the development of AMR, causing the cytotoxic effects of this type of medication to be at the same level as the antifungal effects and forcing the search for compounds that can continue implementing the mechanism of action of azoles but with minimal or less cytotoxicity.

In this sense, metal complexes or coordination compounds have recently aroused much interest in the scientific community, which generate changes in some chemical properties of the active compounds, also providing new possible routes of action, such as more effective delivery of active compounds [20–22]. These metal complexes have shown additional mechanisms of action, such as increased membrane penetration by increased lipophilicity, inhibition of the exchange of some enzymes with enzymatic ligands or substrates, and induction of oxidative stress by the generation of reactive oxygen species, among others [23–29]. These enhanced characteristics possessed by metal complexes make them potential candidates for new compounds with antimicrobial activity that could prevent or reduce the problem of antimicrobial resistance. In addition to the requirement that the metal centers possess potential antimicrobial activity, they must be biocompatible and bioavailable, where copper and cobalt stand out [30, 31].

Computational calculations based on density functional theory (DFT) have played an important role in recent years, supporting the structural study of coordination compounds, as well as their antimicrobial activities. From these calculations, it has been possible to evaluate the chemical reactivity of these compounds, as well as to identify their physicochemical and electronic characteristics and properties [32–34]. By carrying out these computational studies, it has been possible to establish the possible geometries of the coordination compounds, the distribution of electronic densities throughout the complex, the energetic differences between the molecular orbitals (frontier molecular orbitals analysis) and to elucidate the possible interactions of those with different cell areas (enzymes, cell wall and membrane, among others).

Herein, we report the synthesis and characterization of four new coordination complexes containing Co(II) and Cu(II) as metal centers and ligands derived from benzotriazole and we tested the bioactivity on fluconazole-resistant isolates of *Candida* species and reference strains, epidemiologically relevant. This aim was achieved by exploring the effect of these metal complexes on planktonic growth and two major virulence traits as well as yeast-to-hyphae transition and biofilm growth. In addition, we assayed the antiproliferative activity in murine macrophages to know the selectivity of the coordination complexes synthesized here. Such assays are pivotal to characterize and estimate the promissory value of these molecules for further development of inorganic medicinal chemistry targeting biologically relevant and versatile metallic complexes.

Murcia-Galán *et al. BMC Chemistry*   (2023) 17:135

Page 3 of 21

Results and discussion

Synthesis of 1,3-bis(benzotriazol-1-yl)-propan-2-ol (1)

Several tests were performed using the previously reported methods from literature [35], though it was impossible to duplicate the synthetic procedure to obtain **1**. As a result, this article presents an alternative synthesis route consisting of a phase-transfer catalyzed coupling reaction between 1,3-dichloro-propan-2-ol and 1*H*-benzotriazol followed by thin-layer chromatography (Additional file 1: Figure S42).

Compared to the work reported by Zhang *et al.* the product was separated as a white, air-stable solid with a higher yield. Elemental analysis, FT-IR, Raman spectroscopy, ^{1}H, and ^{13}C NMR were used to characterize **1**, allowing for a highly pure identification of the ligand.

Synthesis and characterization of metal complexes

The complexes were synthesized using either a pure solvent or a mixture of solvents that could dissolve both the ligand and the corresponding metallic salts. In order to produce **2** and **3**, the reaction was carried out in acetone, where immediate precipitation of the complexes was observed. This solvent was also used to wash the end products. Due to the polar protic solvent affinity
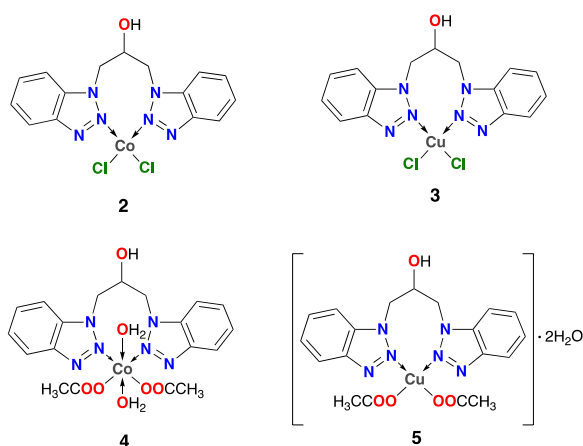

Fig. 1 Possible structures of the complexes under study

for metallic salts in cases **4** and **5**, a solvent mixture was required. Tetrahydrofuran and methanol form the solvent mixture, where the product is kept in solution and removing the solvent at the end of the reaction is necessary. All the complexes (**2**–**5**) were isolated as non-hygroscopic and air-stable solids. Figure 1 shows the proposed structures of the complexes under investigation.

Furthermore, **2**–**5** only show significant solubility in polar protic solvents such as ethanol and methanol. Elemental analysis of the complexes revealed that **5** possess hydration water molecules and **4** likely had water molecules apparently coordinated to the metal core. These statements are supported by thermal analysis.

FTIR spectroscopy

All complexes were studied using infrared spectroscopy (FT-IR) to determine the shifts of specific bands associated with ligand stretching molecular vibrations upon coordination with the metal core. Table 1 provides a summary of the assignment of important bands in the ligand and its complexes.

Relevant groups in the structure of the free ligand (**1**) exhibit distinctive infrared bands. Two stretching bands observed in the FT-IR spectra were related to the alcohol group, with bands at 3368 cm^{-1} and 1092 cm^{-1} assigned to O-H and C-O bonds, respectively. The C-H stretching band found at 3067 cm^{-1} was assigned to the aromatic system (found in the benzotriazole moiety), and the band at 2924 cm^{-1} was assigned to aliphatic C-H stretching corresponding to the propan-2-ol spacer. Finally, peaks at 1454 cm^{-1} and 1227 cm^{-1} were assigned to N-N and C-N stretching vibration of the benzotriazole fragment. The coordination of the ligand to a metal center can be confirmed using these peaks most effectively [36, 37].

The metal coordination to the nitrogen of the azole group in **2** and **3** is explained by a shift in the N-N and C-N bands with respect to **1** [38, 39]. Thus, the hypothesized coordination mode in Fig. 1 is validated. While the C-N bond band shifts to 1231 and 1234 cm^{-1} for complexes **2** and **3**, respectively, the N-N bond band shifts

Table 1 Infrared spectral bands for ligand **1** and its complexes

Compound	Wavenumber ν /cm^{-1}						
	(O–H)	(C-H)	(C-H)	(C=O)	(N–N)	(C-N)	(C-O)
1	3368 s	3067 w	2924 w	–	1454 m	1227 vs	1092 s
2	3491 m	3098 w	2928 w	–	1458 m	1231 vs	1026 s
3	3379 m	–	–	–	1458 m	1234 s	1092 m
4	3368 s	3067 w	2924 w	1558 vs	1415 vs	1227 s	1096 m
5	3367 m	3067 w	2920 w	1609 vs	1423 vs	1227 s	1084 m

*w: weak; m: medium; s: strong; vs: very strong

Murcia-Galán *et al. BMC Chemistry*   (2023) 17:135

Page 4 of 21

to 1458 cm^{-1} for both complexes. In the case of **4** and **5**, the C-N bond band does not shift from its position in **1**. However, a larger shift in the band assigned to N–N bond was observed for **4** and **5**, shifting to lower wavenumbers (1415 and 1423 cm^{-1}, respectively). Raman spectroscopy will be used to explain this behavior. However, due to the presence of acetate ligands, compounds **4** and **5** present a new band at 1558 and 1609 cm^{-1} that was attributed to the stretching of the C=O bond. The M-OH$_2$ stretching band was expected to be visible between 1600 and 1630 cm^{-1} [40], but it is masked by bands for the acetate ligand. Raman spectroscopy could be used to observe these bands.

Raman spectroscopy

Compounds **1**–**5** were analyzed by Raman spectroscopy to contribute to their characterization. Table 2

Table 2 Raman spectral bands for **1** and its complexes

Wavenumber/cm^{-1}					
Assignment	Compound				
	1	**2**	**3**	**4**	**5**
ν (M–O$_{(acetate)}$)	–	–	–	74	116
ν (M-Cl)	–	343	375	–	–
δ (triazole ring)	542	539	544	–	542
δ (triazole ring)	620	620	619	615	625
δ (M-L)	–	951	937	930	938
ν (N–N-N triazole ring)	1165	–	1170	1166	1165
δ (triazole ring)	1233	1226	1233	1227	1229
ν (triazole ring)	1379	1388	1373	1385	1379
δ (benzene ring)	1498	1494	1490	1488	1495
δ (benzene ring)	1590	1599	1589	1586	1590
ν (O–H)	3369	–	3448	3367	3335

summarizes the assignment of the selected bands in the spectra of **1**–**5**.

The bands over 3300 cm^{-1} in the ligand and complexes were assigned to the O–H stretching from the propan-2-ol moiety of the ligand. For **1**, bands observed at 1379, 1233, 620, and 542 cm^{-1} were assigned to the triazole ring stretching, breathing, bending, and torsion, respectively [41–44]. Another band of interest is located at 1165 cm^{-1}, which is assigned to the N–N-N symmetric stretching [44, 45]. As a result of the coordination of the metal to the N of the benzotriazole, these bands appear to shift in the complex spectra, suggesting a reduction in the rigidity of the triazole ring. The bands observed at 343 cm^{-1} (**2**) and 375 cm^{-1} (**3**) are assigned to the Co-Cl and Cu-Cl vibration, respectively [46, 47]. While bands observed at 74 cm^{-1} (**4**) and 116 cm^{-1} (**5**) are associated with the bond between the metal center and the oxygen from the acetate co-ligand [48].

Additionally, the bands at 951 cm^{-1} (**2**), 937 cm^{-1} (**3**), 930 cm^{-1} (**4**), and 938 cm^{-1} (**5**) were only observed in the complexes spectra and may be associated with the different interactions between cobalt and copper center and the ligand. Finally, the stretching bands at 1590 and 1498 cm^{-1} in the ligand associated with the benzene ring [41, 43, 45], shifted toward lower wavenumbers in the spectra of the complexes, denoting a decrease in the rigidity of this ring.

UV/Vis spectroscopy

To study electronic properties related to the complex characteristics, the UV–Vis spectra of the compounds were recorded in methanol. The bands for the ligand, complexes **2**–**5**, and metallic salts used for complexation, are shown in Table 3.

All compounds (**1**–**5**) exhibit three bands between 200 and 300 nm, which correspond to $\pi \rightarrow \pi^*$ orbitals

Table 3 Excitation bands for the starting metallic salts, ligand (**1**) and complexes (**2**–**5**) were observed in their UV/Vis spectra

Compound	Transition (nm) (ε(M^{-1} cm^{-1}))					
	UV			Vis		
	λ_1	λ_2	λ_3	λ_1	λ_2	λ_3
1	204 (76,272)	262 (23,597)	280 (16,771)			
2	204 (39,461)	263 (12,404)	280 (9304)	530 (25)		
3	203 (60,623)	262 (17,372)	276 (11,714)	860 (106)		
4	203 (32,949)	261 (10,264)	280 (8426)	514 (28)		
5	204 (49,112)	262 (13,205)	278 (9498)	424 (192)	450 (262)	714 (38)
CoCl$_2$·6H$_2$O	202 (688)	268 (107)		522 (18)		
CuCl$_2$·2H$_2$O	208 (6142)	270 (8163)		896 (66)		
Co(CH$_3$COO)$_2$·4H$_2$O	204 (1031)	268 (47)		518 (14)		
Cu(CH$_3$COO)$_2$·H$_2$O	246 (4269)			698 (94)		

Murcia-Galán *et al. BMC Chemistry*   (2023) 17:135

Page 5 of 21

electronic transitions of the ligand. These very intense bands, which merely changed in intensity, do not exhibit a relevant wavelength shift in the complexes spectra compared to the free ligand spectrum. While cobalt(II) complexes (**2**, **4**) exhibit a blue color in solution and pink color as a solid, copper(II) complexes (**3**, **5**) have a green hue in both the solid and solution phases.

Cobalt(II) salts and their complexes (**2**, **4**) only exhibit one band at 510–530 nm, which could be assigned to the $^4T_{1g}$ (F) ← $^4T_{1g}$ (P) transitions in a distorted octahedral geometry in solution [49, 50]. Bands at 420–900 nm were observed in the spectra of copper(II) salts and their complexes (**3**, **5**), which may be assigned to the single possible transition of the d^9 metal [49, 51]. However, it cannot be specifically attributed to any particular geometry. A bathochromic shift in the bands in the visible region was identified when comparing the spectra of the complexes (**2–5**) with their respective salts.

Thermal analysis

The suggested TG and DTG findings are based on the expected mass losses for all complexes. The stages of decomposition, temperature ranges, and decomposition products, as well as the weight loss percentages of the complexes, are given in Additional file 1: Table S1, all the TGA and DTG data are shown in the Additional file 1.

Upon thermal decomposition, complex **3** produces a final residue containing metal and chlorine, whereas carbon and oxygen are also present in the end residue of complex **2**. A final residue containing metal, carbon, and oxygen was encountered for the other complexes [52–54]. Furthermore, the thermograms show a partial decomposition above 600 °C.

In the case of complex **2**, a weight reduction of 31.63% was observed between 152 and 352 °C, which implies a loss of a fragment of **1** corresponding to one benzotriazole plus one CH_4 equivalent. The decompositions of the remaining benzotriazole fragment and one CH_2 equivalent occurring as three weight loss processes (31.91%) were observed (31.16% calculated). These weight losses leave a metallic residue containing the salt with carbon and oxygen. On the other hand, **3**, suffers a slight weight loss between 27 and 170 °C, which was only possible to link with a small amount of molecular hydrogen. The second loss of 9.25% was observed and assigned to a partial propane fragment. Over 253 °C, a major reduction in weight of 62.14%, was attributed to the loss of two benzotriazole fragments with some additional atoms. Finally, a 3.40% weight drop occurs, leaving a metallic residue.

The thermogram of **4**, shows an initial weight loss between 27 and 239 °C (with the peak temperature for the decomposition stage at 159 °C), which may be related to the loss of a carbon atom and two water molecules coordinated to the metal center, both of which needed high temperatures to be released. The loss of ligand (**1**) is attributed to two decomposition stages that occur at 239–358 and 358-573 °C, with weight losses of 34.10 and 22.81%, respectively. A final weight reduction takes place, leaving a metallic residue with carbon and oxygen, possibly corresponding to a metallic oxide with organometallic features [52–54].

For complex **5**, there is an initial loss that may be related to the removal of two coordination water molecules, similar to complex **4**. Additionally, the loss of the majority of the ligand (**1**) was connected to the second and third decomposition stages with weight reductions of 25.35 and 28.37%, respectively. Finally, a weight reduction of 8.80% is associated with the propan-2-ol fragment, which results in a metallic residue [52–54] similar to the one of **4**. The complexes containing chloride ligands are more stable than those containing acetate ligands. This is supported by the fact that the observed main weight losses of **2** and **3** have a larger maximum DTG and TG range compared to **4** and **5**.

Biological studies

Effect on planktonic cells

Co(II) and Cu(II) complexes containing 1,3-bis(benzotriazol-1-yl)-propan-2-ol, ligand, and its salts were evaluated against *Candida* spp. and mammalian cells. The results of MIC and CFM are detailed in Additional file 1: Table S2.

The ligand (**1**), Cu(II) salts, and Cu(II) complexes (**3** and **5**) did not show a significant inhibitory effect against any of the *Candida* strains evaluated (MIC > 1000 μg mL^{-1}). The Cu(II) center has a dual role, and it is an essential micronutrient to fungal growth and proliferation but also exhibits antimicrobial properties due to the generation of reactive oxygen species [55], which are exploited by the immune cells to kill pathogens through increasing and/or limiting copper levels during infection. *C. albicans* copes with elevated or decreased concentrations of Cu by different mechanisms, such as (1) swapping metal cofactors of superoxide dismutase and increases in expression of transporter CTR1 for Cu uptake [56]; (2) stimulating the expression of copper-transporting P-type ATPase to increase the Cu efflux and 3) chelating copper by expression of metallothioneins [57]. One of these three mechanisms could explain the resistance exhibited by *Candida* strains to copper salts and complexes **3** and **5** tested here.

On the contrary, cobalt(II) salts and their complexes (**2** and **4**) significantly inhibited planktonic cells of *Candida* spp. (MIC 7.81–125 μg mL^{-1}). The antifungal effect of complex **4** on *C. albicans*, *C. tropicalis* and *C. parapsilosis* (reference strain and clinical isolate, MIC 62.5 μg mL^{-1}) was similar; however, *C. glabrata* MYA2950 showed greater sensitivity to both **2** and **4**, compared to the

Murcia-Galán *et al. BMC Chemistry*   (2023) 17:135

Page 6 of 21

CAPF-07 isolate. Likewise, complex **2** exhibited a greater inhibitory effect against fluconazole resistance *C. tropicalis* isolate than its ATCC counterpart (Additional file 1: Table S2). Complex **4** shows better MIC against all *Candida* strains, due to the presence of co-ligand acetate in its structure, which could inhibit biosynthesis pathways of some aminoacids, generate stress in intracellular pH homeostasis, and inhibit the activity of efflux pumps [58, 59]. Importantly, the antifungal activity of the complexes was > 8× greater than the free ligand. The obtained results were compared with the standard drugs FCZ and ITZ according to CLSI protocol.

Most of the studies that evaluate the minimum inhibitory concentration of coordination complexes, test their activity against *Candida albicans*, where it has been found that Co(II) compounds with ligands that contain azoles in their structure present MIC values between 12.5 and 400 µg mL^{-1} [60], 31.25 and 62.5 µg mL^{-1} [61], and 7.8–15.6 µg mL^{-1} [62], showing values close to those obtained with the complexes presented in this work. However, it has been found that these compounds become significantly cytotoxic, and they have even evaluated the possible cause of this effect [62]. Other articles have studied both Co(II) and Cu(II) complexes, presenting the same MIC values against *C. albicans*, 125 µg mL^{-1} [62]. When evaluating the cytotoxicity of Cu(II) complexes, it was found that the concentration at which it is not cytotoxic no longer presents antibiofilm activity [63].

Those studies that have evaluated the antifungal activity against different strains of *Candida* (*C. albicans, C. tropicalis, C. parapsilosis, C. glabrata,* and *C. krusei*), of Co(II) and Cu(II) complexes with azole derivative ligands, have presented MIC values of 15.62–100 µg mL^{-1} (Co complexes) [64], 1.75–50 µg mL^{-1} (Cu complex) [65], and 31.25–250 µg mL^{-1} (Co complexes) [66]. In addition, these complexes showed greater activity against *Candida* non-*albicans* strains, like what was observed with the complexes obtained in this study. In addition, in the present study, it is also observed that the MIC values of the Co(II) complexes present the same activity against sensitive and resistant strains. Several literature reports use the disk diffusion method to test the antifungal activity [67–72], which does not allow comparison with the results presented here. In addition, most articles only carry out biological activity tests against *C. albicans*. In other studies, Co(II) and Cu(II) complexes with ligands derived from isatin and sulfonamides have been reported, in which it has been observed that these present percentages of inhibition between 41 and 77% against strains of *Candida albicans* and *Candida glabrata*, with Co(II) complexes being more active than Cu(II) complexes with both types of ligands [73, 74].

Drug interactions

Interactions between bioactive cobalt(II) complexes (**2** and **4**) and reference drugs (fluconazole and caspofungin) were evaluated on planktonic cells of *C. albicans* and *C. tropicalis* (ATCC strains and clinical isolates). We prioritize these species because they were less susceptible to complexes effects than other strains assayed here. Moreover, they are more prevalent in clinical cases of Candidemia [75]. Indifferent and additive interactions were observed in all the strains studied. However, combinations of MICs of caspofungin and complex **4** were synergistic against *C. tropicalis* 66,029 (FIC caspofungin 0.09 versus FIC complex **4** 0.25; ∑FIC Index 0.34). This combination allowed for a four-fold decrease of the MIC values of complex **4** (62.5 µg mL^{-1} to 15.62 µg mL^{-1}) and caspofungin (0.125 µg mL^{-1} to 0.031 µg mL^{-1}). Additionally, an antagonistic effect was observed on *C. albicans* 90,028 when the MICs of FCZ and complex **4** were combined (FIC FCZ 0.15; FIC C3 6; ∑FIC Index 6.15). The isobolograms of the synergistic and antagonistic combinations are shown in Additional file 1: Figure S41. This finding of synergistic interaction is interesting, since combined therapies could be more effective and less toxic than monotherapies. Explorations of the toxic effect of this combination on mammalian cells must be addressed in future studies to answer if the selectivity index improves.

Effect on virulence traits of Candida spp.

The effect of the cobalt(II) complexes was studied against biofilm and hyphal morphogenesis, two major virulence phenotypes of *Candida* spp, see Fig. 2. The dimorphic switch from yeast to hyphae is considered the transition from the commensal to the pathogenic lifestyle of *C. albicans* [75]. However, yeast and hyphae have different roles during infections. In this way, hyphal growth is an important morphotype to penetration and invasiveness, while the yeast form is related to dissemination [76]. In the present study, we observed that subinhibitory concentrations of complex **2** (31.3 and 62.5 µg/mL) significantly reduced the dimorphic switch in *C. albicans*, while complex **4** did not affect the hyphae growth (Fig. 2a). The dimorphic switch is also related to biofilm biogenesis. The biofilms are a physical and metabolic barrier that *Candida* uses to establish infection, grow on different surfaces (tissue and medical devices), and resist antifungal therapy [77]. Such results indicate that complexes **2** and **4** have an inhibitory effect against established biofilms of ATCC strains and clinical isolates of *C. tropicalis* and *C. parapsilosis* after 24 h of incubation with SMIC$_{50}$ from 31.25 to 62.5 µg mL^{-1}. In contrast, this effect was not observed with the biofilm of *C. albicans*
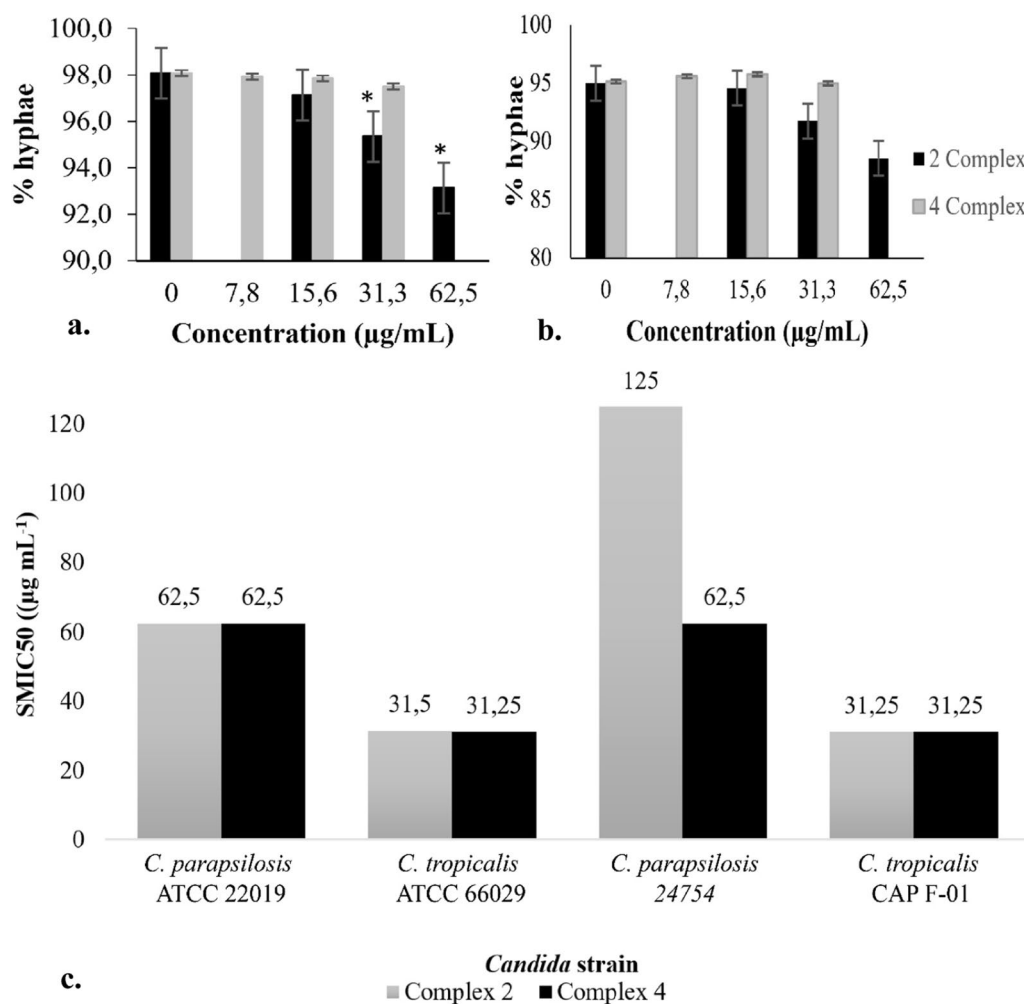
Fig. 2 Inhibition of filamentation by Co(II) complexes (**2**, **4**). Blastospores treated with or without different concentrations of **2** and **4** were incubated in the hyphae-inducing medium at 37 °C, for 4 h. Then, the percent of filamentation and the percent of inhibition was calculated. Bars represent standard error (S.E.). Complexes **2** and **4** inhibited the *C. albicans* ATCC 90028 filamentation in 2.8 and 5%, respectively (**a**), while *C. albicans* CAP F-13 hyphal growth was inhibited in 3.4 and 7.8%, respectively (**b**). *$P < 0.05$. Anti-biofilm activity. Sessile minimum inhibitory concentration 50 (SMIC$_{50}$) of cobalt (II) complexes **2** and **4** on biofilm of *Candida* spp (**c**)

and *C. glabrata* (SMIC$_{50}$ 500- > 2000 µg mL^{-1}), probably due to the differential composition of the biofilm matrix depending on each strain (see Fig. 2b) [17]. Likewise, these results could be explained by the mild suppression (2.8–7.8% of inhibition) of hyphae morphogenesis that was observed in blastospores of *C. albicans* treated with these complexes. Interestingly, *C. tropicalis* biofilm showed higher susceptibility to cobalt complexes independent of the precursor salt used in the synthesis. These results are significant considering that there are no studies reporting the anti-biofilm effect of Co(II) complexes containing 1,3-bis(benzotriazol-1-yl)-propan-2-ol against strains of *Candida* spp. resistant to fluconazole.

Cytotoxicity in vitro

The results are shown in Fig. 3. The ligand, copper(II) complexes (**3, 5**) and its salts did not show to be cytotoxic on murine macrophages (CC$_{50}$ > 90 µg mL^{-1}). However, cobalt(II) complexes (**2, 4**) bioactive on *Candida* spp. and cobalt(II) salt CoCl$_2$·6H$_2$O were partially toxic (CC$_{50}$ 38.87 – 66.7 µg mL^{-1}) with SI between 0.93 -1.44. In the case of complex **2**, the union of the ligand and the salt allowed a decrease of almost twice the CC$_{50}$, contrary to the complexation to form complex **4**, where it was shown to affect the cellular viability in comparison with the salt alone.
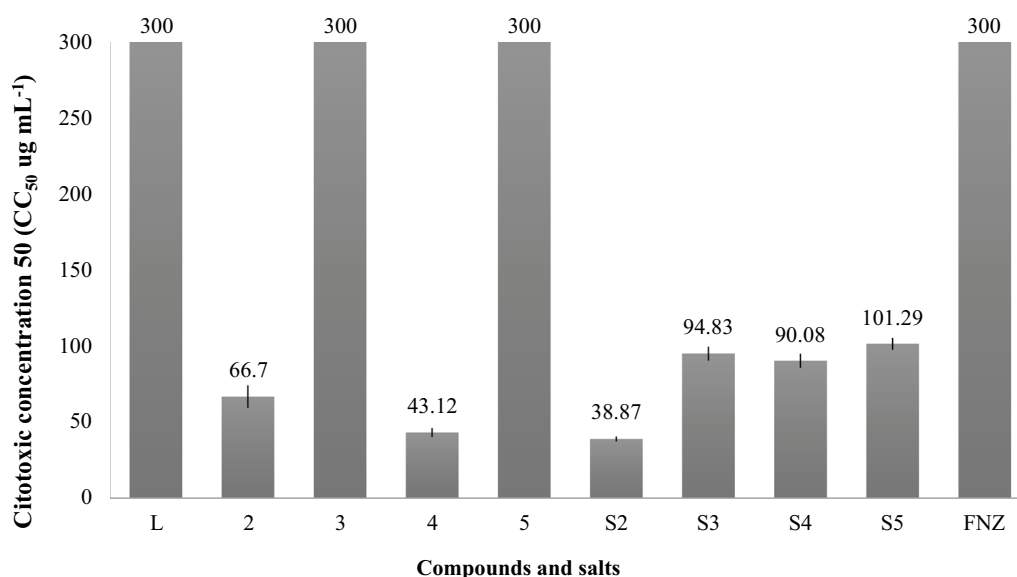
Murcia-Galán *et al. BMC Chemistry*   (2023) 17:135

Page 8 of 21

Fig. 3 Cytotoxicity in macrophages J774.A1 of Co(II) and Cu(II) complexes containing 1,3 bis(benzotriazol-1-yl)-propan-2-ol. **L**: ligand (**1**); S2: $CoCl_2 \cdot 6H_2O$; S3: $CuCl_2 \cdot 2H_2O$; S4: $Co(CH_3COO)_2 \cdot 4H_2O$; S5: $Cu(CH_3COO)_2 \cdot H_2O$; FNZ: fluconazole

DFT calculations

Density functional theory (DFT) calculations were employed in a computational study for complexes **2** and **3**. While **3**, which has a d^9 metal core, only has one conceivable electronic distribution (D, a doublet), **2**, which has a d^7 metal center, has two possible electronic distributions, with either one (D, a doublet) or three (Q, a quadruplet) unpaired electrons. Four distinct conformers were also investigated, considering the different multiplicities of each complex.

The relative bonding energies of the different conformers (a–d) of both complexes at their different electronic distributions at their optimized structures are shown in Table 4. It can be noted that the differences between the different conformers are negligible based on these energies. According to bonding energies, in the case of **2**, the most stable conformers are those with three unpaired electrons. However, the encountered differences do not surpass 1 eV. The structures of the conformers are presented as Additional file 1.

The conformers of **2** and **3**, in a doublet electronic configuration present distorted tetrahedral and square planar geometries, whereas the conformers in a quadruplet electronic configuration only present a distorted tetrahedral geometry. The structural features that give rise to the different conformations considering the bond angles between the metal center and the coordinated chlorine and nitrogen atoms are presented in Table 5. It is observed that the chlorine atoms had greater mobility in comparison to the nitrogen's, whose movement is restricted by the rigidity of the ligand **1**.

Table 4 Relative bond energy of the conformers (a-d) of complexes **2** and **3**, considering different electronic distributions (D=doublet, Q=quadruplet)

Complex/Multiplicity/Conformer		Relative bonding energy (eV)
2	Da	0.28
	Db	0.00
	Dc	0.17
	Dd	0.29
	Qa	0.37
	Qb	0.05
	Qc	0.00
	Qd	0.05
3	Da	0.31
	Db	0.00
	Dc	0.21
	Dd	0.42

The conformers of **2** in a doublet and quadruplet electronic configuration have similar or equal bond lengths between Co center and nitrogen of the ligand, due to the restricted mobility of nitrogen in the ligand; however, the bond length between Co center and each chlorine has a significant difference, 5–8 pm. In these conformers, it is observed that the bond length of the Co–N is lower when the geometry of the conformer is close to the square planar and increases by being closer to the tetrahedral. For the conformers of **3**, it is

Table 5 Bond angles and bond lengths of the conformers of **2** and **3**

Complex/Multiplicity/Conformer		Bond angle (°) and Bond length (pm)					
		N_x-M-Cl_a	N_x-M-Cl_b	N_y-M-Cl_a	N_y-M-Cl_b	N-M-N	Cl-M-Cl
2	Da	93.6	130.8	119.5	100.7	104.6	109.5
		Co-Cl	223.1	217.8	Co-N	200.2	202.6
	Db	117.1	110.3	117.1	110.3	86.8	112.7
		Co-Cl	217.5	223.9	Co-N	205.3	205.3
	Dc	91.8	94.4	91.8	94.4	133.8	164.2
		Co-Cl	219.4	224.7	Co-N	196.4	196.4
	Dd	92.4	90.8	92.4	90.8	157.7	162.8
		Co-Cl	223.7	219.2	Co-N	190.1	190.1
	Qa	102.2	109.8	108.7	107.1	107.2	121.1
		Co-Cl	223.6	218.9	Co-N	207.7	207.4
	Qb	114.3	111.4	114.3	111.4	87.2	115.2
		Co-Cl	218.3	225.9	Co-N	206.9	206.9
	Qc	114.4	111.5	114.4	111.5	86.6	115.3
		Co-Cl	218.0	226.2	Co-N	207.9	207.9
	Qd	111.1	114.1	111.1	114.1	87.1	115.8
		Co-Cl	225.9	218.2	Co-N	207.4	207.4
3	Da	93.0	143.2	125.3	101.7	94.1	104.1
		Cu-Cl	225.4	218.6	Cu-N	213.8	230.6
	Db	125.7	106.6	125.7	106.6	79.1	109.1
		Cu-Cl	217.3	225.5	Cu-N	225.0	225.0
	Dc	91.1	93.1	91.1	93.1	139.4	168.0
		Cu-Cl	223.3	227.5	Cu-N	213.7	213.7
	Dd	94.8	95.6	94.8	95.6	131.1	154.6
		Cu-Cl	228.8	222.3	Cu-N	212.8	212.8

observed a behavior like the conformers of complex **2**, except for **3Da**; this has different bond lengths for each Cu–N, which is related to the tetrahedral geometry that is more distorted than for others.

With the aim of gaining a deeper understanding of the electronic structure of these complexes, a Natural Bond Orbital (NBO) analysis was performed. The natural population analysis (NPA) gives the population of the natural localized atomic charges for the studied systems at their different electronic states, whose results are presented in Fig. 4. The four top isosurface plots represent the bonding interaction of the respective ligands, with the total corresponding occupation number including the spin α and spin β contributions. In all cases the occupation can be approximated to 2 e, as is expected for a Chloride (Cl^-) anionic donating and lone-donating pairs from nitrogenated (N:) ligands. The bottom isosurface plots represent the unpaired electrons from the metal atoms separated as spin α and spin β. In the case of **2Da** and **2Qa**, a d^7 electron configuration is expected for Co^{2+}, with one unpaired spin α electron for **2Da** and three unpaired spin α electrons for **2Qa**, see Fig. 4. In the case of the copper complex, a

d^9 electron configuration is expected for Cu^{2+}, with one unpaired spin α electron for **3Da,** which is consistent with our findings as presented in Fig. 4.

The spin density of the studied complexes was calculated as the difference between the densities of electrons with spin α and those of spin β, [78] and visualized as double colored isosurfaces as presented in Fig. 5. This demonstrates that the unpaired electrons are localized at the metal centers. Despite of the differences on the electronic configuration between the cobalt and copper complexes, the electrostatic potential map, shows a similar distribution of the electron density, mainly because cobalt and copper in these complexes possess the same +2 charge (see Fig. 5). Into this context, the Hirshfield and Bader charges where calculated, as presented in Table 6. It must be noted that some differences are encountered when comparing both methodologies, the differences comparing the charges of Cl and N atoms directly linked to the metal atoms do not exceed 0.1.

The results obtained from the energy decomposition analysis (EDA) are shown in Table 7, for all the conformers of **2** and **3**. The [$MLCl_2$] complexes (M = Co(II), Cu(II) and L = **1**) were separated into {MCl_2} and {L}

Murcia-Galán *et al. BMC Chemistry*   (2023) 17:135
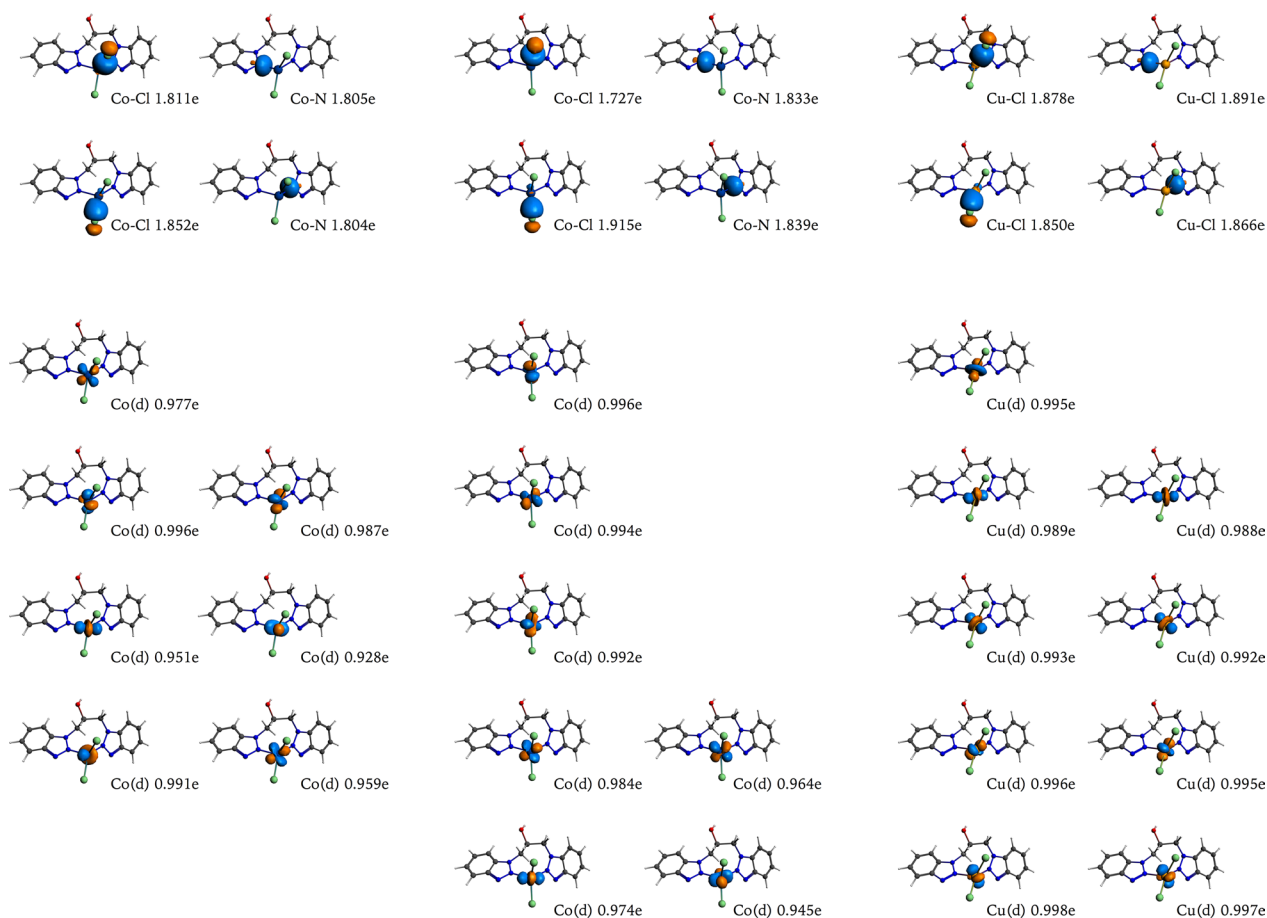
Page 10 of 21

2Da   2Qa   3Da

Fig. 4 Selected NBO with their respective occupation numbers for **2Da**, **2Qa**, and **3Da**, represented using a cutoff isosurface value of 0.070

fragments, whose interaction gives the interaction energy (ΔE_{inter}) for these fragments. The ΔE_{inter} is decomposed into three main terms: Pauli's repulsion (ΔE_{Pauli}), electrostatic interaction (ΔE_{elstat}) and orbital interactions (ΔE_{orb}), the last two can be grouped due to their stabilizing character, determining the ionic and covalent character of the interaction [79].

For **3**, the stabilizing character of all the conformers is mainly due to electrostatic interactions (over 60%), while the orbital interactions only represent 40% of the contribution, with similar interaction energies. **3Da** and **3Db** show that Pauli's repulsion overcompensates the electrostatic interactions; however, **3Dc** and **3Dd** need additional compensation from orbital interactions. The differences encountered are related to the variations in the spatial distribution of ligand **1** and the imposed steric hindrance. Whereas **3Da** and **3Db** present a distorted tetrahedral geometry, **3Dc** and **3Dd**

present a distorted square planar geometry, which has a major repulsion considering the parallel interaction between the two fragments.

In the case of complex **2**, the conformers **2Da**, **2Db**, **2Dc** and **2Dd** show a similar behavior than the conformers of **3**, where the conformers with distorted tetrahedral geometry (**2Da** and **2Db**) generate a lower Pauli's repulsion compared with those of distorted square planar geometry (**2Dc** and **2Dd**). For **2Da** and **2Db**, the major stabilizing contribution corresponds to ΔE_{orb} with a 79.7 and 63.5%, respectively. However, the covalent and ionic nature of the interaction are equivalent (around 50%) for **2Dc** and **2Dd** (see Table 7).

With respect to Pauli's repulsion term, huge differences were found. **2Da** and **2Db,** the orbital interaction term produces a compensation of the ΔE_{Pauli} repulsive term. This is related to the orbital relaxation and the orbital mixing between the fragments which is favored by the
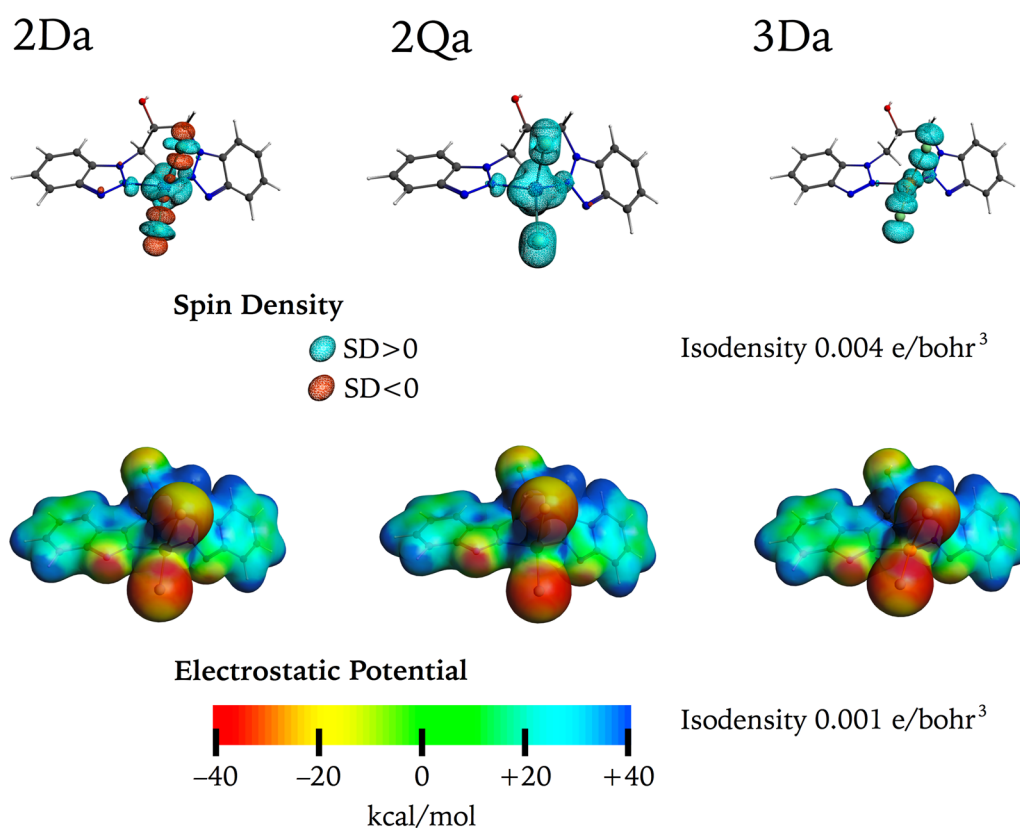
Fig. 5 Top: Spin density for **2 Da**, **2Qa**, and **3 Da** at the isosurface cutoff value of 0.004 e/bohr^3. Bottom: isosurfaces, corresponding to the total electron density using an isosurface cutoff value of 0.001 e/bohr^3 mapped with the electrostatic potential between a range of − 40 and + 40 kcal/mol

Table 6 Hirshfield and Bader charges for **2** and **3**

Atom*	2Da		2Qa		3Da	
	Hirshfield	**Bader**	**Hirshfield**	**Bader**	**Hirshfield**	**Bader**
M	0.104	0.996	0.153	1.082	0.325	0.876
Cl	− 0.233	− 0.528	− 0.265	− 0.583	− 0.295	− 0.515
Cl	− 0.229	− 0.497	− 0.266	− 0.550	− 0.288	− 0.44
N	0.018	− 0.191	0.017	− 0.209	− 0.025	− 0.139
N	0.020	− 0.199	0.017	− 0.184	− 0.015	− 0.151

*Up and down references are referred to the structures presented in Figs. 4 and 5

angles at which the interaction occurs. Additionally, the larger Pauli's repulsion contribution for **2Dc** and **2Dd** is overcompensated with both stabilizing interactions ΔE_{elstat} and ΔE_{orb}.

On the other hand, the orbital interactions are the main stabilizing factor of the {MCl$_2$}-{L} interaction in **2Qa**, **2Qb**, **2Qc,** and **2Qd**. All these conformers present the same distorted tetrahedral geometry, as well as **2Da** and **2Db**.

Moreover, the MD simulation results show that at 300 K, the **2** complex in its doublet and quartet state (**2Da** and **2Qa**) behave as rigid system, in which the **2** complexes show their breathing mode during simulation, which is more pronounced for **2Qa** (see Fig. 6). For **3Da**, a larger variation in the < msd > is shown, compared to the **2Da** and **2Qa** configurations. However, these variations do not exceed 0.3 Å along the complete simulation, confirming that do there is no change in the coordination

Murcia-Galán *et al. BMC Chemistry*   (2023) 17:135

Page 12 of 21

Table 7 Energy Decomposition Analysis (EDA) of the {MCl$_2$}-{L} interaction for the different conformers of **2** and **3**. Values in kJ·mol^{-1}

Complex/ Multiplicity/ Conformer		ΔE_{inter}	ΔE_{Pauli}	ΔE_{elstat}†	ΔE_{orb}†
2	Da	− 1513.54	688.25	− 440.36 (20.3%)	− 1733.92 (79.7%)
	Db	− 573.49	565.24	− 406.01 (36.5%)	− 707.27 (63.5%)
	Dc	− 384.33	1190.07	− 757.67 (49.2%)	− 783.27 (50.8%)
	Dd	− 466.85	1022.25	− 782.93 (53.9%)	− 669.57 (46.1%)
	Qa	− 650.34	545.76	− 480.03 (41.0%)	− 689.43 (59.0%)
	Qb	− 404.45	739.62	− 516.56 (46.2%)	− 602.05 (53.8%)
	Qc	− 932.62	699.69	− 470.15 (29.3%)	− 1136.50 (70.7%)
	Qd	− 546.11	564.53	− 467.82 (43.1%)	− 617.38 (56.9%)
3	Da	− 179.88	360.29	− 321.95 (61.6%)	− 200.72 (38.4%)
	Db	− 184.29	327.88	− 297.86 (61.1%)	− 189.76 (38.9%)
	Dc	− 167.52	619.87	− 454.44 (60.3%)	− 299.02 (39.7%)
	Dd	− 184.97	596.00	− 448.37 (59.9%)	− 300.23 (40.1%)

† Values in parentheses give the percentage contribution to the total attractive interactions ($\Delta E_{Electrostatic} + \Delta E_{Orbital}$)

modes of the complexes. Thus, according to the EDA analyzes, it is confirmed that the **2Da** is more rigid due to its larger covalent character.

In summary, considering the total bonding energy interaction and its decomposition into three main terms, **2Da** is the most favored conformer, with a large contribution from the orbital interactions and a distorted tetrahedral geometry that favored the formation of a bond between the metal center and the ligand (**1**) with main covalent character. In the case of **3**, all conformers present similar interaction energy, where the main stabilization contribution possesses an ionic character. Additionally, the MD simulations confirm that there exists a fluxional behavior that does not allow us to identify the favored conformer but confirms that the structure proposed is stable during the simulation time.

Conclusions

In conclusion, one ligand derived from benzotriazole was synthesized employing a different methodology to that reported in the literature. Furthermore, four new complexes of Co(II) and Cu(II) were obtained from this ligand, which was characterized by spectroscopic, elemental, and thermogravimetric techniques. All the complexes (**2**–**5**) had 1:1 (*M:L*) stoichiometries based on characterization data, where **2** and **3** had tetrahedral geometry, while **4** and **5** had octahedral geometry.
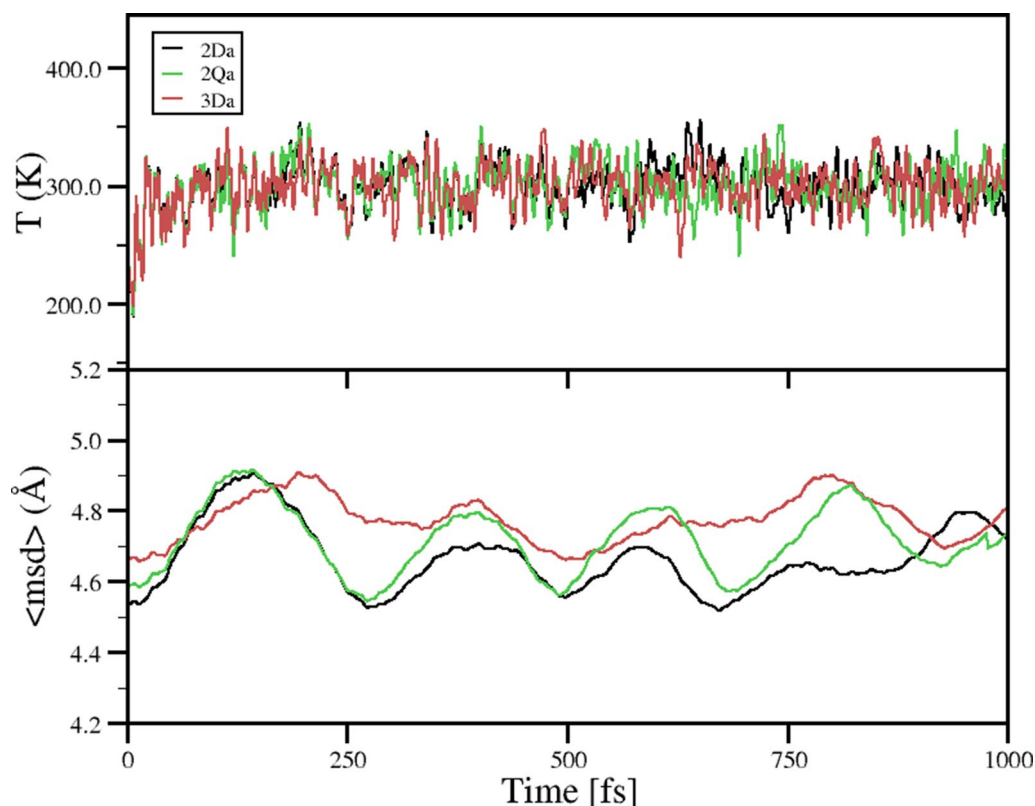

Fig. 6 Temperature (T) and mean square displacement ⟨msd⟩ during molecular dynamics simulation for **2Da**, **2Qa**, and **3Da** complexes at 300 K, respectively

DFT calculations were carried out to propose the probable structures for **2** and **3**, where conformer **2Da** was selected as the possible geometry, while conformers of 3 had a fluxional behavior that does not allow a clear possible geometry. The findings highlight the promising role of Co(II) complexes containing 1,3-bis(benzotriazol-1-yl)-propan-2-ol as antifungal agents capable of reducing the dimorphic change in *C. albicans* and biofilm of non-*albicans* species sensitive and resistant to fluconazole. In addition, combination therapies can be examined in the future to improve selectivity in mammalian cells because synergistic interactions with caspofungin were also observed.

Materials and methods

General information

The metallic salts $CoCl_2 \cdot 6H_2O$ (purity, 98%), $CuCl_2 \cdot 2H_2O$ (purity, 99%), $Co(CH_3COO)_2 \cdot 4H_2O$ (purity, 98%) and $Cu(CH_3COO)_2 \cdot H_2O$ (purity, 98%) were used as received from Alfa Aesar. The compounds 1H-benzotriazole (purity, 99%), 1,3-dichloro-propan-2-ol (purity, 98%), and tetrabutylammonium bromide (purity, 98%) were purchased from Sigma-Aldrich and were used as received.

Elemental analysis (C, H, and N) was performed with a Thermo Scientific™ FLASH 2000 CHNS/O Analyzer. Fourier transform infrared (FTIR) spectra were recorded on a Thermo Nicolet NEXUS FTIR spectrophotometer using ATR module. Melting points were determined on a Mel-Temp® 1101D apparatus in open capillary tubes and are uncorrected. Ultraviolet/visible (UV/vis) spectra were recorded on an Agilent Technologies Cary 100 spectrophotometer in DMSO from 200 to 800 nm in a quartz cuvette with a path length of 1 cm. Raman spectroscopy was performed in a RIBA Yovin-Ivon spectrometer using a laser with a wavelength of 786 nm. Thermogravimetric (TG) analyses of the complexes were conducted on a NETZSCH STA 409 PC/PG by evaluating 8–10 mg samples of the complexes in a nitrogen atmosphere. Samples were subjected to dynamic heating over a temperature range of 30–700 °C at a heating rate of 10 °C min⁻¹. TG curves were analyzed to obtain the percent mass losses as a function of temperature. Nuclear magnetic resonance (NMR) spectra were recorded on a Bruker AscendTM-400 spectrometer at 295 K. Chemical shifts are reported in ppm relative to SiMe₄ (¹H) as an internal standard. ¹H and ¹³C NMR chemical shifts (δ) are reported in parts per million (ppm) relative to TMS, with the residual solvent peak used as an internal reference; $CDCl_3$ (¹H NMR δ: 7.26 and ¹³C NMR δ: 77.2) and DMSO-d_6 (¹H NMR δ: 2.50 and ¹³C NMR δ: 39.5). High-resolution mass spectrometry (HRMS) data was obtained on an Agilent Technologies Q-TOF 6520 spectrometer via electrospray ionization (ESI) in positive ion mode.

Synthesis of 1,3-bis(benzotriazol-1-yl)-propan-2-ol (1)

In a Schlenk tube equipped with a reflux condenser, 1H-benzotriazole (2.500 g; 20.99 mmol), potassium hydroxide (1.211 g; 21.58 mmol), tetrabutylammonium bromide (0.997 g; 3.09 mmol), and water (20 mL) were stirred at 55 °C for 45 min. Then, 1,3-dichloro-propan-2-ol (1.0 mL; 1.390 g; 10.78 mmol) and toluene (40 mL) were added, and the mixture was heated for 48 h at 85°C. A white solid was generated at the interface; therefore, the reaction mixture was allowed to cool at room temperature (rt) and filtered under vacuum. The filtrate was extracted with 4 portions of water (20 mL), separated and dried with sodium sulfate. The solution was concentrated to dryness under vacuum to give a yellow solid. Both solids were mixed and purified by recrystallization with tetrahydrofuran:pentane and the ligand was obtained as a white solid (structure of the ligand **1** is shown in Fig. 7 with the respective atom numbering).

Yield 2.225 g (72.03%). M.p.: 185–187 °C. FTIR (ATR, cm⁻¹): 3368 (OH), 3067 (C-H), 2924 (C-H), 1616, 1589, 1497, 1454 (N–N), 1420, 1358, 1304, 1281, 1265, 1227 (C-N), 1169, 1134, 1092 (C-O), 1038, 1011, 922, 872, 849, 799, 779, 768, 737, 667, 625, 606, 575, 548, 517, 471, 428. Raman (cm⁻¹): 3369 (O–H), 3314, 3168, 3071, 2991, 2950, 2918, 1762, 1590 (benzene ring), 1498 (benzene ring), 1379 (triazole ring), 1270, 1233 (triazole ring), 1165 (N–N-N, triazole ring), 1122, 1003, 879, 768, 620 (triazole ring), 542 (triazole ring), 331, 181.

¹H NMR (400.1 MHz, DMSO-d_6) δ 8.04 (d, 2H, 4, 4'), 7.91 (d, 2H, 7, 7'), 7.56 (t, 2H, 6, 6'), 7.40 (t, 2H, 5, 5'), 5.62 (d, 1H, OH), 4.99 (dd, 2H, 2, 2'), 4.81 (dd, 2H, 2, 2'), 4.56 (s, 1H, 1). ¹³C NMR (DMSO-d_6, 101 MHz) δ 145.15 (C3, C3'), 133.78 (C8, C8'), 127.17 (C6, C6'), 123.89 (C5, C5'), 119.04 (C4, C4'), 111.26 (C7, C7'), 68.90 (C1), 51.41(C2, C2'). MS–ESI (m/z, ES+) calcd. For $[M+H]^+$: 295, found: 295. UV/Vis bands λ_{max}, nm (ε, L mol⁻¹ cm⁻¹): 204 (76,272), 262 (23,597), 280 (16,771). Anal. Calcd. for $C_{15}H_{14}N_6O$: C 61.21; H 4.79; N 28.55. Found: C 61.25; H 4.84; N 28.49%.
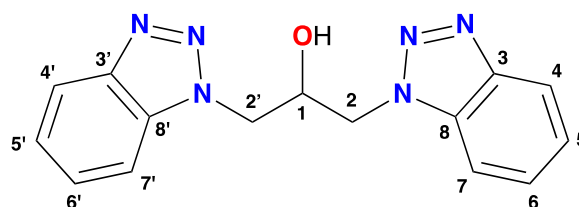

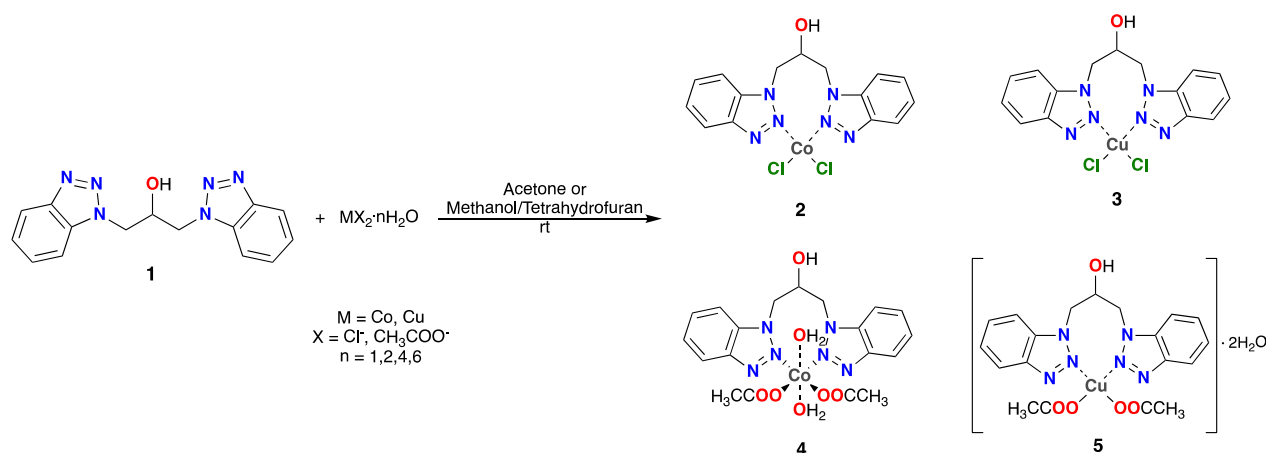**Fig. 7** Atom numbering for signal assignment of the ¹H and ¹³C NMR for **1**

Murcia-Galán *et al. BMC Chemistry*   (2023) 17:135

Page 14 of 21

Fig. 8 General procedure of synthesis of complexes (**2**–**5**)

Synthesis of the complexes

The general procedure for the synthesis of complexes (**2**–**5**) is shown in Fig. 8.

Synthesis of [Co{1,3-bis(benzotriazol-1-yl)-propan-2-ol-N,N} Cl₂] (2)

(**1**) (0.35 mmol; 103.4 mg) was dissolved in acetone (17 mL), and CoCl₂·6H₂O (0.34 mmol; 80.9 mg) in acetone (5 mL) was added to this mixture. The resulting solution was stirred for 3 h at rt. This mixture was centrifuged at 400 rpm for 9 min, washing with acetone and ethyl ether removing the liquid phase between each wash. Then, the solvent was evaporated to dryness to give a blue solid.

Yield: 132.2 mg (91.7%). M.p.: 341–346 °C (decomposition). FTIR (ATR, cm⁻¹): 3491 (O–H), 3098 (C–H), 2928 (C–H), 1709, 1597, 1497, 1458 (N–N), 1435, 1393, 1373, 1350, 1312, 1288, 1231 (C-N), 1184, 1169, 1146, 1026 (C-O), 949, 876, 853, 806, 779, 756, 741, 671, 621, 579, 540, 521, 428. Raman (cm⁻¹): 3074, 2968, 2933, 2920, 1599 (benzene ring), 1494 (benzene ring), 1388 (triazole ring), 1364, 1293, 1226 (triazole ring), 1126, 1008, 951 (M-L), 875, 775, 664, 620 (triazole ring), 571, 539 (triazole ring), 497, 466, 343 (M-Cl), 304, 193. UV/Vis bands λ_{max}, nm (ε, L mol⁻¹ cm⁻¹): 204 (39,461), 263 (12,404), 280 (9304), 530 (25). Anal. Calcd. for C₁₅H₁₄Cl₂CoN₆O: C 42.48; H 3.33; N 19.81. Found: C 42.51; H 3.39; N 19.78%.

Synthesis of [Cu{1,3-bis(benzotriazol-1-yl)-propan-2-ol-N,N} Cl₂] (3)

(**1**) (0.34 mmol; 99.6 mg) was dissolved in acetone (14 mL), and CuCl₂·2H₂O (0.33 mmol; 55.9 mg) in acetone (8 mL) was added to this mixture. The resulting solution was stirred for 3 h at rt. This mixture was centrifuged at 400 rpm for 9 min, washing with acetone

and ethyl ether removing the liquid phase between each wash. Then, the solvent was evaporated to dryness to give a pea-green solid.

Yield: 95.8 mg (67.7%). M.p.: 195–199 °C (decomposition). FTIR (ATR, cm⁻¹): 3379 (O–H), 1593, 1493, 1458 (N–N), 1323, 1288, 1234 (C-N), 1165, 1092 (C-O), 1003, 945, 872, 779, 745, 667, 652, 575, 513, 432. Raman (cm⁻¹): 3448 (O–H), 3329, 3293, 3172, 3070, 2946, 1751, 1589 (benzene ring), 1490 (benzene ring), 1456, 1373 (triazole ring), 1281, 1233 (triazole ring), 1170 (N–N-N, triazole ring), 1126, 997, 937 (M-L), 876, 777, 619 (triazole ring), 544 (triazole ring), 375 (M-Cl), 265. UV/Vis bands λ_{max}, nm (ε, L mol⁻¹ cm⁻¹): 203 (60,623), 262 (17,372), 276 (11,714), 860 (106). Anal. Calcd. for C₁₅H₁₄Cl₂CuN₆O: C 42.02; H 3.29; N 19.60. Found: C 42.05; H 3.31; N 19.55%.

Synthesis of [Co{1,3-bis(benzotriazol-1-yl)-propan-2-ol-N,N} (H₂O)₂(CH₃COO)₂] (4)

(**1**) (0.34 mmol; 100.3 mg) was dissolved in tetrahydrofuran:methanol (4:1, 15 mL), and Co(CH₃COO)₂·4H₂O (0.34 mmol; 83.7 mg) in tetrahydrofuran:methanol (3:2, 5 mL) was added to this mixture. A color change of the solution to orange was immediately observed. The resulting solution was stirred for 2 h at rt. The solution was concentrated to dryness under a vacuum to give a purple solid, which was washed with acetone and ethyl ether, removing the liquid phase between each wash. Then, the solvent was evaporated to dryness to give a purple solid.

Yield: 131.1 mg (76.0%). M.p.: 162–166 °C (decomposition). FTIR (ATR, cm⁻¹): 3367 (O–H), 3067 (C-H), 2924 (C-H), 1558 (C=O), 1497, 1416 (N–N), 1342, 1304, 1227 (C-N), 1165, 1134, 1096 (C-O), 1015, 872, 779, 741, 667, 613, 548, 513, 471, 432. Raman (cm⁻¹): 3367 (O–H), 3062, 2989, 2947, 2917, 1586 (benzene ring), 1488 (benzene ring), 1451,

Murcia-Galán *et al. BMC Chemistry*   (2023) 17:135

Page 15 of 21

1385 (triazole ring), 1308, 1267, 1227 (triazole ring), 1166 (N–N-N, triazole ring), 1109, 998, 930 (M-L), 878, 772, 615 (triazole ring), 179, 74 (M–O$_{(acetate)}$). UV/Vis bands λ$_{max}$, nm (ε, L mol^{-1} cm^{-1}): 203 (32,949), 261 (10,264), 280 (8426), 514 (28). Anal. Calcd. for C$_{19}$H$_{24}$CoN$_6$O$_7$: C 44.98; H 4.77; N 16.56. Found: C 44.99; H 4.80; N 16.53%.

Synthesis of [Cu{1,3-bis(benzotriazol-1-yl)-propan-2-ol-N,N} (CH₃COO)₂]· 2H₂O (5)

(**1**) (0.34 mmol; 100.5 mg) was dissolved in tetrahydrofuran:methanol (4:1, 15 mL), and Cu(CH$_3$COO)$_2$·H$_2$O (0.33 mmol; 66.8 mg) in tetrahydrofuran:methanol (3:2, 5 mL) was added to this mixture. The resulting solution was stirred for 5 h at reflux. The reaction mixture was allowed to cool at rt and concentrated to dryness under vacuum to give a green solid, which was washed with acetone and ethyl ether removing the liquid phase between each wash. Then, the solvent was evaporated to dryness to give a dark green solid.

Yield: 156.1 mg (93.1%). M.p.: 199–203 °C (decomposition). FTIR (ATR, cm^{-1}): 3368 (O-H), 3067 (C-H), 2920 (C-H), 1609 (C=O), 1497, 1423 (N-N), 1300, 1281, 1227 (C-N), 1165, 1134, 1084 (C-O), 1003, 934, 899, 872, 779, 745, 683, 625, 548, 513, 432. Raman (cm^{-1}): 3335 (O-H), 3173, 3066, 2928, 1590 (benzene ring), 1532, 1495 (benzene ring), 1447, 1379 (triazole ring), 1287, 1267, 1229 (triazole ring), 1165 (N-N-N, triazole ring), 1122, 1003, 938 (M-L), 884, 838, 775, 698, 625 (triazole ring), 542 (triazole ring), 511, 302, 220, 186, 116 (M–O$_{(acetate)}$). UV/Vis bands λ$_{max}$, nm (ε, L mol^{-1} cm^{-1}): 204 (49,112), 262 (13,205), 278 (9498), 424 (192), 450 (262), 714 (38). Anal. Calcd. for C$_{19}$H$_{24}$CuN$_6$O$_7$: C 44.57; H 4.72; N 16.41. Found: C 44.62; H 4.81; N 16.31%.

Biological studies
Microorganisms and mammalian cells
The study was carried out on eight strains of *Candida* spp. Four reference strains obtained from the American Type Culture Collection-ATCC (*C. albicans* 90,028; *C. tropicalis* 66,029; *C. glabrata* MYA2950; *C. parapsilosis* 22,019) and clinical isolates resistant to fluconazole donated and characterized genotypically and phenotypically by Corporación para Investigaciones Biológicas—CIB, Medellín, Colombia (*C. albicans* CAPF-13; *C. tropicalis* CAPF-01; *C. glabrata* CAPF-07; *C. parapsilosis* 24,754). All yeasts were cultured on saboraud agar (OXOID Ltd., Basingstoke, Hampshire, UK) at 35 °C. Fresh cultures were used for each experiment.

Macrophage J774.A1 (ATCC® TIB-67™) was donated by Cellular and Functional Biology and Biomolecular Engineering Group from the Universidad Antonio Nariño, Colombia. The cells were cultured in Dulbecco's modified Eagle's medium (DMEM) (Gibco, USA), supplemented with 10% inactivated fetal bovine serum (Gibco, USA), 1% penicillin–streptomycin (Gibco, USA) and kept under conditions of 95% humidity, 5% CO$_2$ and 37 °C.

Susceptibility on planktonic cells of Candida sp
The minimum inhibitory concentrations (MICs) for strains of *Candida* spp were determined by the microdilution method according to Clinical & Laboratory Standards Institute (CLSI) guidelines, protocol M27-A4. Fluconazole (FCZ) and itraconazole (ITZ) obtained from Sigma-aldrich were used as reference drugs. The minimum fungicidal concentration (CFM) was determined from subcultures on saboraud agar of the MIC and concentrations above the MIC. The CFM was the concentration of the compound in which the growth of ≤ 3 CFU was observed after 24 h of incubation at 35 ºC.

In vitro drug interaction assay
The modified fixed-ratio isobologram method described by Quinton L. Fivelman *et al.* was used [80]. Pharmacological interactions between drug A and drug B were prepared from MIC. Concentrations equal to 8X MIC, 4X MIC, 2X MIC, MIC, 1/2 MIC, and 1/4 MIC were prepared and combined inversely (Additional file 1: Table S3).

U-bottom plates were inoculated with 0.5×10^2 cells/mL—2.5×10^3 cells/mL of *Candida* spp. incubated for 24 h, 37 °C. Fractional MICs were obtained visually as the concentration that inhibits 50% of the initial inoculum. Fractional inhibitory concentrations (FIC) are calculated from the MIC obtained using Eq. (1).

$$FIC(drug) = \frac{MIC(drug\ in\ combination)}{MIC(drug\ alone)} \tag{1}$$

The $\sum$FIC index is obtained from the sum of the FIC of the drugs in each combination. Its value defines whether the interaction is synergistic (< 0.5), additive (0.51—0.99), indifferent (1—3.9), or antagonistic (> 4).

Antibiofilm activity
To evaluate the effect of cobalt(II) complexes on the resulting biofilm, 10^6 cells/ml of *Candida* spp. were grown in RPMI 1640. 200 µL of each culture was added to 96-well flat-bottom microtiter plates and incubated for 24 h at 37 °C with shaking (50 rpm) to allow biofilm formation as was previously described [81]. Afterward, *Candida* biofilms were rinsed three times with PBS to remove planktonic cells. Different concentrations of cobalt (II) complexes were added to yield final concentrations among 1/2MIC-4XMIC. Plates were incubated without shaking for 24 h, at 37 °C. Untreated cells and RPMI 1640 without yeast were included as positive and

Murcia-Galán *et al. BMC Chemistry*   (2023) 17:135

Page 16 of 21

negative controls, respectively. The metabolic activity of biofilms was determined using a semi-quantitative 2,3-bis-(2-methoxy-4-nitro-5-sulfophenyl)-2H-tetrazolium-5-carboxanilide (XTT, Cayman Chemical) reduction assay. In brief, stock solutions of XTT in PBS (0.5 g/L) and Menadione in acetone (10 mM) were prepared and stored at -80 °C. Prior to use XTT/menadione solutions were freshly prepared in a ratio 10:1. 100 µL of XTT/Menadione mixture was then added to each well. Plates were incubated for 3 h, at 37 °C, in the dark, and absorbance was measured at 490 nm. The sessile minimum inhibitory concentrations ($SMIC_{50}$) were calculated.

Filamentation assay

The inhibitory effect of Co(II) complexes on the switch from yeast to hyphae of *C.l albicans* was tested, according to described by Sun *et al.*, 2015 [82]. Briefly, cells were grown at 37 °C on YPD broth (1% yeast extract, 2% peptone, and 2% glucose), with rotary shaking at 200 rpm, overnight. Then, cells were harvested by centrifugation and washed twice with ultrapure water. 2.5×10^6 cells/mL were transferred to RPMI 1640 supplemented with 0.5% GlcNAc; 0.5% peptone, and 0.3% KH_2PO_4, with or without metallic complexes (control). The compounds were added in a concentration range of 7.8–62.5 µg/mL. The plates were incubated at 37 °C during 4 h. Lastly, cell morphology was recorded by counting at least 200 cells, discriminating between yeast cells and hyphae. The results were expressed as the percentage of the mycelium, and the inhibition percent was calculated. Ten repetitions were established with each concentration. The assays were repeated in two independent moments.

In vitro cytotoxicity assay

The in vitro effect of the complexes, ligands, and salts on the viability of J774.A1 macrophages was determined by the colorimetric method using the tetrazolium salt (3-(4,5-dimethylthiazol-2-yl)-2,5-diphenyltetrazolium bromide (MTT, Sigma-Aldrich). In summary, a cell density of 1×10^5 cells/mL in monolayer was exposed for 72 h with the metal complexes in concentration ranges 300–11.1 µg/mL. Then, MTT was added to each well (10%) for 4 h, and the optical density determined at 595 nm using an iMark™ Microplate Absorbance Reader (BioRad, Madrid, Spain). The cytotoxicity percentage was calculated with the equation: [(OD450nm control–OD450nm treatment)/OD450nm treatment)] $\times 100$. The results were expressed as Cytotoxic Concentration 50 (CC_{50}) determined by sigmoidal regression using Msxlfit software (GO Business Solution, Guildford, UK) [83–85].

Statistical analysis

Data analysis of filamentation assays was performed with the statistical package IBM SPSS Statistics 25.0. The effect of different concentrations of Co(II) complexes on dimorphic transition of *C. albicans* were determined using the Kruskal–Wallis test. A *p* value < 0.05 was defined as statistically significant. The cytotoxic concentration 50 (CC_{50}) and 90 (CC_{90}) were calculated by sigmoidal regression from the percentages of inhibition using Msxlfit software (GO Business Solution, Guildford, UK). Graphs were generated using Microsoft Excel.

Computational details
Density functional theory calculations

The Amsterdam Density Functional (ADF) package [86] was used to calculate geometrical, electronic structures, and optical properties at the relativistic level of theory. A spin-unrestricted scheme was employed for open shell systems. The scalar relativistic effects were incorporated into the calculations by means of a two-component Hamiltonian with the zeroth-order regular approximation (ZORA) [87, 88]. The generalized gradient approximation (GGA) with the exchange–correlation functional by Perdew-Burke-Ernzerhof (PBE) [89, 90] was used for all calculations. Additionally, the triple-ζ quality Slater-type orbital (STO) basis set with one polarization functions (TZP) and two polarization functions (TZ2P) [91] were used for non-metallic (H, C, N, O and Cl) and metallic atoms (Co and Cu), respectively. Finally, the Stefan Grimme dispersion correction functional (GRIMME3) with Becke and Johnson damping function (BJDAMP) [92–94] were included for all calculations.

According to the experience of authors specialized in DFT calculation, the most suitable methodology to address the Cobalt and Copper complexes present in this manuscript correspond to SR-PBE-D3BJ/TZP-TZ2P. In this sense, benchmark studies show that PBE including vdW corrections is a suitable functional to study inorganic complexes [95, 96]. To account for weak interactions, dispersion corrections were included in these calculations, mainly due to the different conformations that ligands can adopt, since the metal center has a positive charge which reduces the effective number of electrons for the dispersion interactions. The Perdew–Burke–Ernzerhof (PBE) density functional was chosen based in previous literature studies [97–102].

Spin Density of the studied complexes was calculated as the difference between the densities of electrons with spin α and those of spin β, and visualized as double colored isosurfaces [78]. Population analyses were carried out on the basis of the natural population analysis (NPA) scheme by using the NBO5 standalone suite [103]. Also,

the Hirshfield analysis, that generates a charge value by comparing the integral of the charge density over space weighted by the relative fraction of the (initial) density of that fragment in the total initial (sum-of-fragments) density [104, 105]. Finally, a real-space partition of the electronic density based on the quantum theory of atoms in molecules (QTAIM) developed by Richard Bader was employed as implemented in ADF [106].

Energy decomposition analysis (EDA)

The bonding analysis focuses on the interaction energy of a bond formed between two fragments in a specific electronic state with a frozen geometry. In the case of the complexes studied here, the complexes [MCl$_2$L] were fragmented in {MCl$_2$} and {L} corresponding to ligand (**1**), and their electronic energy and wavefunctions were obtained by performing single-point calculations. Subsequently, the fragment's wavefunctions were combined to obtain the molecular wavefunction and corresponding binding interaction energy [107]. The EDA scheme proposed by Morokuma-Ziegler [108–111], dissects the binding interaction energy into three main components: electrostatic interaction, Pauli's repulsion, and orbital interaction (see Eq. (2)).

$$\Delta E_{inter} = \Delta E_{elstat} + \Delta E_{Pauli} + \Delta E_{orb} \qquad (2)$$

The electrostatic component (ΔE_{elstat}) corresponds to the classical interaction form, the superposition of the unperturbed fragment densities at the molecular geometry, considering the effects associated with Coulombic attraction and repulsion. This component has a stabilizing character. The Pauli's component (ΔE_{Pauli}) is associated with the principle through explicit antisymmetrization and renormalization of the product wavefunction and the energy change between the superposition of the unperturbed wavefunction of the isolated fragment and the molecular wavefunction of the conformer. The Pauli's term has a destabilizing character. Finally, the orbital mixing component (ΔE_{orb}) has a stabilizing influence due to the mixing of occupied and unoccupied orbitals that generate a relaxation of the molecular system and can involve charge transfer and polarization effects [107].

Molecular dynamics (MD) simulations

In order to explore the thermodynamic stability of **2Da** and **3Da** complexes, we have carried out Molecular dynamics MD simulations as implemented in the Orca quantum chemistry package [112]. We have used the default Velocity Verlet algorithm in the NVT ensemble at the PBE/def2-SVP level of theory. A Timestep of 0.5 femtoseconds and initial velocities according to a temperature of 300 K are used. Temperature is maintained at 300 K using a Berendsen thermostat [113]. The

simulations are performed for a time of 30 ps with 10 fs of time step. The behavior of the mean square displacement ⟨msd⟩ as a function of time allows us to determine the average bond-length variations during MD simulation. In order to analyze the temperature stability of **2Da** and **3Da** complexes, we evaluated the mean-square displacement ⟨msd⟩ defined in Eq. (3).

$$< msd >= \frac{1}{N} \sum_{i=1}^{N} [r_i(t) - r_i(0)]^2 \qquad (3)$$

where r$_i$(t) is the position vector of the i-th atom at the time t and N is the total number of atoms in the system. The dynamical behavior of boron clusters has been rationalized by the ⟨msd⟩ parameter [114]. In a rigid system, the ⟨msd⟩ parameter remains constant, whereas in a non-rigid system the ⟨msd⟩ show variations as a function of the time.

Supplementary Information

The online version contains supplementary material available at https://doi.org/10.1186/s13065-023-01037-7.

> **Additional file 1.** Additional figures and tables.

Author contributions
RAM-G carried out the synthesis and characterization of the ligand and complexes. SMD, JDV, LVH and TWN performed the in vitro experiments. RAM-G, AM-C and DM-C carried out the DFT computational calculus. PLR-K carried out the MD simulations. RAM-G, JJH, SML and MVR write the original draft. All authors contributed with crucial discussions and constructive reviews. JJH is the corresponding author.

Availability of data and materials
No datasets were generated or analyzed during the current study.

Declarations

Ethics approval and consent to participate
Not applicable.

Consent for publication
Not applicable.

Competing interests
The authors declare that they have no competing interests.

Author details
¹Grupo de Investigación en Química Inorgánica, Catálisis y Bioinorgánica, Departamento de Química, Universidad de los Andes, Carrera 1 No. 18A-12, 111711 Bogotá, Colombia. ²Facultad de Ciencias Médicas y de la Salud, Universidad de Santander, Calle 70 No. 55-210, Bucaramanga, Colombia.

Murcia-Galán *et al. BMC Chemistry*   (2023) 17:135

Page 18 of 21

[3]Grupo Sistema Estomatognático Y Morfofisiología (SEMF), Departamento de Ciencias Básicas, Universidad Santo Tomás Seccional Bucaramanga, Carrera 27 No. 180-395, Bucaramanga, Colombia. [4]Facultad de Ingeniería, Arquitectura y Diseño, Universidad San Sebastián, Bellavista 7, 8420524 Santiago, Chile. [5]Facultad de Ingeniería, Instituto de Ciencias Químicas Aplicadas, Inorganic Chemistry and Molecular Materials Center, Universidad Autónoma de Chile, El Llano Subercaseaux 2801, Santiago, Chile. [6]Experimental and Medical Micology Group, Corporación para Investigaciones Biológicas (CIB), 050010 Medellin, Colombia. [7]Facultad de Medicina, Universidad Pontificia Bolivariana, 050034 Medellín, Colombia. [8]Centro de Investigaciones en Óptica A.C., Loma del Bosque 115, Col. Lomas del Campestre, 37150 León, Guanajuato, México.

References

1. Ferri M, Ranucci E, Romagnoli P, Giaccone V. Antimicrobial resistance: a global emerging threat to public health systems. Crit Rev Food Sci Nutr. 2017;57(13):2857–76. https://doi.org/10.1080/10408398.2015.1077192.

2. Roca I, Akova M, Baquero F, Carlet J, Cavaleri M, Coenen S, Cohen J, Findlay D, Gyssens I, Heure OE, Kahlmeter G, Kruse H, Laxminarayan R, Liébana E, López-Cerero L, MacGowan A, Martins M, Rodríguez-Baño J, Rolain JM, Segovia C, Sigauque B, Tacconelli E, Wellington E, Vila J. The global threat of antimicrobial resistance: science for intervention. New Microbes New Infect. 2015;6:22–9. https://doi.org/10.1016/j.nmni.2015.02.007.

3. Murray CJ, Ikuta KS, Sharara F, Swetschinski L, Aguilar GR. Global burden of bacterial antimicrobial resistance in 2019: a systematic analysis. The Lancet. 2022;399(10325):629–55. https://doi.org/10.1016/S0140-6736(21)02724-0.

4. Woolhouse M, Ward M, Van Bunnik B, Farrar J. Antimicrobial resistance in humans, livestock and the wider environment. Philos Trans R Soc B: Biol Sci. 2015;370(1670):1–7. https://doi.org/10.1098/rstb.2014.0083.

5. Ayukekbong JA, Ntemgwa M, Atabe AN. The threat of antimicrobial resistance in developing countries: causes and control strategies. Antimicrob Resist Infect Control. 2017;6(1):1–8. https://doi.org/10.1186/s13756-017-0208-x.

6. Marston HD, Dixon DM, Knisely JM, Palmore TN, Fauci AS. Antimicrobial resistance. JAMA. 2016;316(11):1193–204. https://doi.org/10.1001/jama.2016.11764.

7. Limper AH, Adenis A, Le T, Harrison TS. Fungal infections in HIV/AIDS. Lancet Infect Dis. 2017;17(11):e334–43. https://doi.org/10.1016/S1473-3099(17)30303-1.

8. Kandati J, Boorsu S, Ponugoti M, Samudrala V. Bacterial and fungal agents causing lower respiratory tract infections in patients with human immunodeficiency virus infection. Int J Res Med Sci. 2016;4(8):3595–600. https://doi.org/10.18203/2320-6012.ijrms20162335.

9. Feldman C, Anderson R. Bacterial respiratory infections complicating human immunodeficiency virus. Semin Respir Crit Care Med. 2016;37(2):214–29. https://doi.org/10.1055/s-0036-1572558.

10. Antachopoulos C, Walsh TJ, Roilides E. Fungal infections in primary immunodeficiencies. Eur J Pediatr. 2007;166(11):1099–117. https://doi.org/10.1007/s00431-007-0527-7.

11. Pilmis B, Puel A, Lortholary O, Lanternier F. New clinical phenotypes of fungal infections in special hosts. Clin Microbiol Infect. 2016;22(8):681–7. https://doi.org/10.1016/j.cmi.2016.05.016.

12. Revie NM, Iyer KR, Robbins N, Cowen LE. Antifungal drug resistance: evolution, mechanisms and impact. Curr Opin Microbiol. 2018;45:70–6. https://doi.org/10.1016/j.mib.2018.02.005.

13. Zavrel M, White TC. Medically important fungi respond to azole drugs: an update. Future Microbiol. 2015;10(8):1355–73. https://doi.org/10.2217/FMB.15.47.

14. Perlin DS, Shor E, Zhao Y. Update on antifungal drug resistance. Curr Clin Microbiol Rep. 2015;2:84–95. https://doi.org/10.1007/s40588-015-0015-1.

15. Beardsley J, Halliday CL, Chen SC, Sorrell TC. Responding to the emergence of antifungal drug resistance: perspectives from the bench and the bedside. Future Microbiol. 2018;13(10):1175–91. https://doi.org/10.2217/fmb-2018-0059.

16. Cavalheiro M, Teixeira MC. Candida biofilms: threats, challenges, and promising strategies. Front Med. 2018;5(28):1–15. https://doi.org/10.3389/fmed.2018.00028.

17. Polke M, Hube B, Jacobsen ID. Candida survival strategies. Adv Appl Microbiol. 2015;91:139–235. https://doi.org/10.1016/bs.aambs.2014.12.002.

18. Maertens JA. History of the development of azole derivatives. Clin Microbiol Infect. 2004;10:1–10. https://doi.org/10.1111/j.1470-9465.2004.00841.x.

19. Allen D, Wilson D, Drew R, Perfect J. Azole antifungals: 35 years of invasive fungal infection management. Expert Rev Anti Infect Ther. 2015;13(6):787–98. https://doi.org/10.1586/14787210.2015.1032939.

20. Renfrew AK. Transition metal complexes with bioactive ligands: mechanisms for selective ligand release and applications for drug delivery. Metallomics. 2014;6(8):1324–35. https://doi.org/10.1039/c4mt00069b.

21. Claudel M, Schwarte JV, Fromm KM. New antimicrobial strategies based on metal complexes. Chemistry. 2020;2(4):849–99. https://doi.org/10.3390/chemistry2040056.

22. Noreen S, Sumrra SH. Aminothiazole-linked metal chelates: synthesis, density functional theory, and antimicrobial studies with antioxidant correlations. ACS Omega. 2021;6(48):33085–99. https://doi.org/10.1021/acsomega.1c05290.

23. Lemire JA, Harrison JJ, Turner RJ. Antimicrobial activity of metals: mechanisms, molecular targets and applications. Nat Rev Microbiol. 2013;11(6):371–84. https://doi.org/10.1038/nrmicro3028.

24. Rizzotto M. In: Bobbarala V (ed) A Search for Antibacterial Agents, 1st ed. InTech, Croatia; 2012.

25. Lin Y, Betts H, Keller S, Cariou K, Gasser G. Recent developments of metal-based compounds against fungal pathogens. Chem Soc Rev. 2021;50(18):10346–402. https://doi.org/10.1039/D0CS00945H.

26. Aljohani FS, Omran OA, Ahmed EA, Al-Farrag ES, Elkady EF, Alharbi A, El-Metwaly NM, Barnawi IO, Abu-Dief AM. Design, structural inspection of new bis(1H-benzo[*d*]imidazol-2-yl)methanone complexes: biomedical applications and theoretical implementations via DFT and docking approaches. Inorg Chem Commun. 2023;148:110331. https://doi.org/10.1016/j.inoche.2022.110331.

27. El-Lateef HMA, Khalaf MM, Shehata MR, Abu-Dief AM. Fabrication, DFT calculation, and molecular docking of two Fe(III) imine chelates as anti-COVID-19 and pharmaceutical drug candidate. Int J Mol Sci. 2022;23:3994. https://doi.org/10.3390/ijms23073994.

28. Aljohani ET, Shehata MR, Abu-Dief AM. Design, synthesis, structural inspection of Pd2+, VO2+, Mn2+, and Zn2+ chelates incorporating ferrocenyl thiophenol ligand: DNA interaction and pharmaceutical studies. Appl Organomet Chem. 2021;35:e6169. https://doi.org/10.1002/aoc.6169.

29. Abu-Dief AM, Abdel-Rahman LH, Abdelhamid AA, Marzouk AA, Sehata MR, Bakheet MA, Almaghrabi OA, Nafady A. Synthesis and characterization of new Cr(III), Fe(III) and Cu(II) complexes incorporating multisubstituted aryl imidazole ligand: Structural, DFT, DNA binding, and biological implications. Spectrochim Acta A Mol Biomol Spectrosc. 2020;228:117700. https://doi.org/10.1016/j.saa.2019.117700.

30. O'Shea D. Synthesis, characterisation and biological activity of novel carboxylate complexes incorporating phenanthroline and benzimidazole ligands, Doctoral thesis, Dublin Institute of Technology, Irlanda; 2004. https://arrow.tudublin.ie/tourdoc/2/. Accessed 21 Jun 2022

31. Chang EL, Simmers C, Knight DA. Cobalt complexes as antiviral and antibacterial agents. Pharmaceuticals. 2010;3(6):1711–28. https://doi.org/10.3390/ph3061711.

32. Noreen S, Sumrra SH, Chohan ZH, Mustafa G, Imran M. Synthesis, characterization, molecular docking and network pharmacology of bioactive metallic sulfonamide-isatin ligands against promising drug targets. J Mol Struct. 2023;1277:134780. https://doi.org/10.1016/j.molstruc.2022.134780.

33. Noreen S, Sumrra SH. Correlating the charge transfer efficiency of metallic sulfa-isatins to design efficient NLO materials with better drug designs. Biometals. 2022;35(3):519–48. https://doi.org/10.1007/s10534-022-00385-6.

Murcia-Galán *et al. BMC Chemistry*   (2023) 17:135

Page 19 of 21

34. Sumrra SH, Zafar W, Javed H, Zafar M, Hussain MZ, Imran M, Nadeem MA. Facile synthesis, spectroscopic evaluation and antimicrobial screening of metal endowed triazole compounds. Biometals. 2021;34:1329–51. https://doi.org/10.1007/s10534-021-00345-6.

35. Zhang GF, Dou YL, She JB, Yin MH. Synthesis and crystal structure of a copper coordination polymer [(Cu(btapo)$_2$BrCH$_3$OH)$^+$Br$^-$]$_n$ (btapo = 1,3-bis(benzotriazol-1-yl) propan-2-ol). J Chem Crystallogr. 2006;37:63–7. https://doi.org/10.1007/s10870-006-9152-y.

36. Katritzky AR. Handbook of heterocyclic chemistry. 3rd ed. Amsterdam: Elsevier; 2010.

37. Larkin PJ. Infrared and Raman spectroscopy: principles and spectral interpretation. Amsterdam: Elsevier; 2011.

38. Castillo KF, Bello-Vieda NJ, Nuñez-Dallos NG, Pastrana HF, Celis AM, Restrepo S, Hurtado JJ, Ávila AG. Metal complex derivatives of azole: A study on their synthesis, characterization, and antibacterial and antifungal activities. J Braz Chem Soc. 2016;27:2334–47. https://doi.org/10.5935/0103-5053.20160130.

39. Sandoval-Rojas AP, Ibarra I, Cortés MT, Macías MA, Suescun L, Hurtado J. Synthesis and characterization of copper(II) complexes containing acetate and N, N-donor ligands, and their electrochemical behavior in dopamine detection. J Electroanal Chem. 2017;805:60–7. https://doi.org/10.1016/j.jelechem.2017.10.018.

40. Socrates G. Infrared and Raman characteristic group frequencies: tables and charts. 3rd ed. Chichester: Wiley; 2001.

41. Cao PG, Yao JL, Zheng JW, Gu RA, Tian ZQ. Comparative study of inhibition effects of benzotriazole for metals in neutral solutions as observed with surface-enhanced Raman spectroscopy. Langmuir. 2002;18(1):100–4. https://doi.org/10.1021/la010575p.

42. Yao JL, Ren B, Huang ZF, Cao PG, Gu RA, Tian ZQ. Extending surface Raman spectroscopy to transition metals for practical applications IV A study on corrosion inhibition of benzotriazole on bare Fe electrodes. Electrochim Acta. 2003;48(9):1263–71. https://doi.org/10.1016/s0013-4686(02)00834-4.

43. Honesty NR, Gewirth AA. Shell-isolated nanoparticle enhanced Raman spectroscopy (SHINERS) investigation of benzotriazole film formation on Cu(100), Cu(111), and Cu(poly). J Raman Spectrosc. 2011;43(1):46–50. https://doi.org/10.1002/jrs.2989.

44. Mennucci MM, Banczek EP, Rodrigues PRP, Costa I. Evaluation of benzotriazole as corrosion inhibitor for carbon steel in simulated pore solution. Cem Concr Compos. 2009;31(6):418–24. https://doi.org/10.1016/j.cemconcomp.2009.04.005.

45. Thomas S, Venkateswaran S, Kapoor S, D'Cunha R, Mukherjee T. Surface enhanced Raman scattering of benzotriazole: a molecular orientational study. Spectrochim Acta A Mol Biomol Spectrosc. 2004;60(1–2):25–9. https://doi.org/10.1016/s1386-1425(03)00213-0.

46. Applegarth LM, Corbeil CR, Mercer DJ, Pye CC, Tremaine PR. Raman and ab initio investigation of aqueous Cu (I) chloride complexes from 25 to 80° C. J Phys Chem B. 2014;118(1):204–14. https://doi.org/10.1021/jp406580q.

47. Chukanov NV, Vigasina MF. Raman Spectra of Minerals. In: Vibrational (Infrared and Raman) Spectra of Minerals and Related Compounds. Springer Mineralogy, Springer Nature, Switzerland, 2020. https://doi.org/10.1007/978-3-030-26803-9_4

48. Otero V, Sanches D, Montagner C, Vilarigues M, Carlyle L, Lopes JA, Melo MJ. Characterisation of metal carboxylates by Raman and infrared spectroscopy in works of art. J Raman Spectrosc. 2014;45(11–12):1197–206. https://doi.org/10.1002/jrs.4520.

49. Cotton FA, Wilkinson G, Murillo CA, Bochmann M. Advanced inorganic chemistry. 6th ed. USA-England: John Wiley and Sons; 1999.

50. Titiš J, Hudák J, Kožíšek J, Krutošíková A, Moncol'J, Tarabová D, Boča R. Structural, spectral and magnetic properties of carboxylato cobalt(II) complexes with heterocyclic N-donor ligands: reconstruction of magnetic parameters from electronic spectra. Inorganica Chim Acta. 2012;388:106–13. https://doi.org/10.1016/j.ica.2012.03.036.

51. Deswal Y, Asija S, Kumar D, Jindal DK, Chandan G, Panwar V, Saroya S, Kumar N. Transition metal complexes of triazole-based bioactive ligands: synthesis, spectral characterization, antimicrobial, anticancer and molecular docking studies. Res Chem Intermed. 2022;48:703–29. https://doi.org/10.1007/s11164-021-04621-5.

52. Abdel-Rahman LH, Abu-Dief AM, Ismael M, Mohamed MAA, Hashem NA. Synthesis, structure elucidation, biological screening, molecular modeling and DNA binding of some Cu(II) chelates incorporating imines derived from amino acids. J Mol Structure. 2016;1103:232–44. https://doi.org/10.1016/j.molstruc.2015.09.039.

53. Adam MSS, Abdel-Rahman LH, Abu-Dief AM, Hashem NA. Synthesis, catalysis, antimicrobial activity, and DNA interactions of new Cu(II)-Schiff base complexes. Inorg Nano-Met Chem. 2020;50(3):136–50. https://doi.org/10.1080/24701556.2019.1672735.

54. Abu-Dief AM, Abdel-Rahman LH, Newair EF, Hashem NA. Structure explication, biological evaluation, DNA interaction, electrochemistry and antioxidant activity of iron(II) tri- and tetra-dentate schiff base amino acid complexes. Sohag J Sci. 2021;6(2):9–25. https://doi.org/10.18576/sjs/060201.

55. García-Santamarina S, Thiele DJ. Copper at the fungal pathogen-host axis. J Biol Chem. 2015;290(31):18945–53. https://doi.org/10.1074/jbc.R115.649129.

56. Li CX, Gleason JE, Zhang SX, Bruno VM, Cormack BP, Culotta VC. Candida albicans adapts to host copper during infection by swapping metal cofactors for superoxide dismutase. Proc Natl Acad Sci. 2015;112(38):E5336–42. https://doi.org/10.1073/pnas.1513447112.

57. Schwartz JA, Olarte KT, Michalek JL, Jandu GS, Michel SL, Bruno VM. Regulation of copper toxicity by Candida albicans GPA2. Eukaryot Cell. 2013;12(7):954–61. https://doi.org/10.1128/EC.00344-12.

58. Vasile Scăețeanu G, Chifiriuc M, Bleotu C, Kamerzan C, Măruțescu L, Daniliuc C, Maxim C, Calu L, Olar R, Badea M. Synthesis, structural characterization, antimicrobial activity, and in vitro biocompatibility of new unsaturated carboxylate complexes with 2,2′-bipyridine. Molecules. 2018;23(1):157–74. https://doi.org/10.3390/molecules23010157.

59. Nair MS, Upadhyaya I, Amalaradjou MAR, Venkitanarayanan K. Antimicrobial Food Additives and Disinfectants. In: Singh OM, editor. Foodborne Pathogens and Antibiotic Resistance. USA: John Wiley & Sons; 2017. (**10.1002/9781119139188.ch12**).

60. Apohan E, Yilmaz U, Yilmaz O, Serindag A, Kücükbay H, Yesilada O, Baran Y. Synthesis, cytotoxic and antimicrobial activities of novel cobalt and zinc complexes of benzimidazole derivatives. J Organomet Chem. 2017;828:52–8. https://doi.org/10.1016/j.jorganchem.2016.11.020.

61. Radha VP, Kirubavathy SJ, Chitra S. Synthesis, characterization and biological investigations of novel Schiff base ligands containing imidazoline moiety and their Co(II) and Cu(II) complexes. J Mol Structure. 2018;1165:246–58. https://doi.org/10.1016/j.molstruc.2018.03.109.

62. Fudulu A, Olar R, Maxim C, Scăețeanu GV, Bleotu C, Matei L, Chifiriuc MC, Badea M. New cobalt (II) complexes with imidazole derivatives: antimicrobial efficiency against planktonic and adherent microbes and in vitro cytotoxicity features. Molecules. 2021;26(1):55. https://doi.org/10.3390/molecules26010055.

63. Calu L, Badea M, Korosin NC, Chifiriuc MC, Bleotu C, Stanica N, Silvestro L, Maurer M, Olar R. Spectral, thermal and biological characterization of complexes with a Schiff base bearing triazole moiety as potential antimicrobial species. J Therm Anal Calorim. 2018;134:1839–50. https://doi.org/10.1007/s10973-018-7871-x.

64. Dias BB, da Silva Dantas FG, Galvao F, Cupozak-Pinheiro WJ, Wender H, Pizzuti L, Rosa PP, Tenório KV, Gatto CG, Negri M, Casagrande GA, de Oliveira KMP. Synthesis, structural characterization, and prospects for new cobalt (II) complexes with thiocarbamoyl-pyrazoline ligands as promising antifungal agents. J Inorg Biochem. 2020;213:111277. https://doi.org/10.1016/j.jinorgbio.2020.111277.

65. Stevanović NL, Aleksic I, Kljun J, Skaro Bogojevic S, Veselinovic A, Nikodinovic-Runic J, Turel I, Djuran MI, Glišić BĐ. Copper(II) and Zinc(II) complexes with the clinically used fluconazole: comparison of antifungal activity and therapeutic potential. Pharmaceuticals. 2021;14(1):24. https://doi.org/10.3390/ph14010024.

66. Murcia RA, Leal SM, Roa MV, Nagles E, Muñoz-Castro A, Hurtado JJ. Development of antibacterial and antifungal triazole Chromium(III) and Co(II) complexes: synthesis and biological activity evaluations. Molecules. 2018;23(8):2013. https://doi.org/10.3390/molecules23082013.

67. Ravindran R, Minitha R, Fazil S, Devi AS. Synthesis, spectroscopic and biological studies of metal complexes of an ONO donor pyrazolylhydrazone – Crystal structure of ligand and Co(II) complex. J Indian Chem Soc. 2022;99:100389. https://doi.org/10.1016/j.jics.2022.100389.

68. Obaleye JA, Ajibola AA, Bernardus VB, Hosten EC. Synthesis, X-ray crystallography, spectroscopic and in vitro antimicrobial studies of a

Murcia-Galán *et al. BMC Chemistry*   (2023) 17:135

Page 20 of 21

new Cu(II) complex of trichloroacetic acid and imidazole. J Mol Struct. 2020;1203:127435. https://doi.org/10.1016/j.molstruc.2019.127435.

69. Kalarani R, Sankarganesh M, Vinoth-Kumar GG, Kalanithi M. Synthesis, spectral, DFT calculation, sensor, antimicrobial and DNA binding studies of Co(II), Cu(II) and Zn(II) metal complexes with 2-amino benzimidazole Schiff base. J Mol Structure. 2020;1206:127725. https://doi.org/10.1016/j.molstruc.2020.127725.

70. Sumrra SH, Kausar S, Raza MA, Zubair M, Zafar MN, Nadeem MA, Mughal EU, Chohan ZH, Mushtaq F, Rashid U. Metal based triazole compounds: their synthesis, computational, antioxidant, enzyme inhibition and antimicrobial properties. J Mol Structure. 2018;1168:202–11. https://doi.org/10.1016/j.molstruc.2018.05.036.

71. Ali AE, Elasala GS, Ibrahim RS. Synthesis, characterization, spectral, thermal analysis and biological activity studies of metronidazole complexes. J Mol Structure. 2019;1176:673–84. https://doi.org/10.1016/j.molstruc.2018.08.095.

72. Gaber M, El-Wakiel N, Hemeda OM. Cr(III), Mn(II), Co(II), Ni(II) and Cu(II) complexes of 7-((1H-benzo[d]imidazole-2-yl)diazinyl)-5-nitroquinolin-8-ol. Synthesis, thermal, spectral, electrical measurements, molecular modeling and biological activity. J Mol Structure. 2019;1180:318–29. https://doi.org/10.1016/j.molstruc.2018.12.006.

73. Khalid S, Sumrra SH, Chohan ZH. Isatin endowed metal chelates as antibacterial and antifungal agents. Sains Malays. 2020;49(8):1891–904. https://doi.org/10.17576/jsm-2020-4908-11.

74. Rani S, Sumrra SH, Chohan ZH. Metal based sulfanilamides: a note on their synthesis, spectral characterization, and antimicrobial activity. Russ J Gen Chem. 2017;87:1834–42. https://doi.org/10.1134/S1070363217080331X.

75. McCarty TP, White CM, Pappas PG. Candidemia and invasive candidiasis. Infect Dis Clin. 2021;35(2):389–413. https://doi.org/10.1016/j.idc.2021.03.007.

76. Talapko J, Juzbašić M, Matijević T, Pustijanac E, Bekić S, Kotris I, Škrlec I. Candida albicans—the virulence factors and clinical manifestations of infection. J Fungi. 2021;7(2):79. https://doi.org/10.3390/jof7020079.

77. Mayer FL, Wilson D, Hube B. Candida albicans pathogenicity mechanisms. Virulence. 2013;4(2):119–28. https://doi.org/10.4161/viru.22913.

78. Savarese M, Brémond É, Ciofini I, Adamo C. Electron spin densities and density functional approximations: open-shell polycyclic aromatic hydrocarbons as case study. J Chem Theory Comput. 2020;16(6):3567–77. https://doi.org/10.1021/acs.jctc.0c00059.

79. Zhao L, von Hopffgarten M, Andrada DM, Frenking G. Energy decomposition analysis. Wiley Interdiscip Rev Comput Mol Sci. 2017;8(3):e1345. https://doi.org/10.1002/wcms.1345.

80. Fivelman QL, Adagu IS, Warhurst DC. Modified fixes-ratio isobologram method for studying in vitro interactions between atovaquone and proguanil or dihydroartemisinin against drug-resistan strains of *Plasmodium falciparum*. Antimicrob Agents Chemother. 2004;48(11):4097–102. https://doi.org/10.1128/AAC.48.11.4097-4102.2004.

81. Pierce CG, Uppuluri P, Tummala S, Lopez-Ribot JL. A 96 well microtiter plate-based method for monitoring formation and antifungal susceptibility testing of candida albicans biofilms. J Vis Exp. 2010;44:e2287. https://doi.org/10.3791/2287.

82. Sun L, Liao K, Wang D. Effects of magnolol and honokiol on adhesion, yeast-hyphal transition, and formation of biofilm by Candida albicans. PLoS ONE. 2015;10(2):e0117695. https://doi.org/10.1371/journal.pone.0117695.

83. Abu-Dief AM, Abdel-Rahman LH, Abd-El Sayed MA, Zikry MM, Nafady A. Green synthesis of AgNPs[0] Utilizing *Delonix Regia* extract as anticancer and antimicrobial agents. ChemistrySelect. 2020;5(42):13263–8. https://doi.org/10.1002/slct.202003218.

84. Saddik MS, Elsayed MMA, Abdelkader MSA, El-Mokhtar MA, Abdel-Aleem JA, Abu-Dief AM, Al-Hakkani MF, Farghaly HS, Abou-Taleb HA. Novel green biosynthesis of 5-fluorouracil chromium nanoparticles using *Harpullia pendula* extract for treatment of colorectal cancer. Pharmaceutics. 2021;13(2):226. https://doi.org/10.3390/pharmaceutics13020226.

85. Abu-Dief AM, Alrashedee FMM, Emran KM, Al-Abdulkarim HA. Development of some magnetic metal-organic framework nano composites for pharmaceutical applications. Inorg Chem Commun. 2022;138:109251. https://doi.org/10.1016/j.inoche.2022.109251.

86. Vrije Universiteit SCM. Theoretical chemistry. SCM, 2014. ADF2014, SCM, Theoretical Chemistry, Vrije Universiteit, Amsterdam, The Netherlands, (see http://www.scm.com)

87. Van Lenthe EV, Snijders JG, Baerends EJ. The zero-order regular approximation for relativistic effects: The effect of spin–orbit coupling in closed shell molecules. J Chem Phys. 1996;105(15):6505–16. https://doi.org/10.1063/1.472460.

88. Van Lenthe E, Van Leeuwen R, Baerends EJ, Snijders JG. Relativistic regular two-component Hamiltonians. Int J Quantum Chem. 1996;57(3):281–93. https://doi.org/10.1002/(SICI)1097-461X(1996)57:3%3c281::AID-QUA2%3e3.0.CO;2-U.

89. Perdew JP, Burke K, Wang Y. Generalized gradient approximation for the exchange-correlation hole of a many-electron system. Phys Rev B. 1996;54(23):16533. https://doi.org/10.1103/PhysRevB.54.16533.

90. Perdew JP, Burke K, Ernzerhof M. Generalized gradient approximation made simple. Phys Rev Lett. 1996;77(18):3865. https://doi.org/10.1103/PhysRevLett.77.3865.

91. Van Lenthe E, Baerends EJ. Optimized Slater-type basis sets for the elements 1–118. J Comput Chem. 2003;24(9):1142–56. https://doi.org/10.1002/jcc.10255.

92. Grimme S, Antony J, Ehrlich S, Krieg H. A consistent and accurate ab initio parametrization of density functional dispersion correction (DFT-D) for the 94 elements H-Pu. J Chem Phys. 2010;132(15):154104. https://doi.org/10.1063/1.3382344.

93. Johnson ER, Becke AD. A post-Hartree–Fock model of intermolecular interactions. J Chem Phys. 2005;123(2):024101. https://doi.org/10.1063/1.1949201.

94. Grimme S, Ehrlich S, Goerigk L. Effect of the damping function in dispersion corrected density functional theory. J Comput Chem. 2011;32(7):1456–65. https://doi.org/10.1002/jcc.21759.

95. Chen L, Janssens TV, Grönbeck H. A comparative test of different density functionals for calculations of NH 3-SCR over Cu-Chabazite. Phys Chem Chem Phys. 2019;21(21):10923–30. https://doi.org/10.1039/C9CP01576K.

96. Naderizadeh B, Bayat M. Nature of metal–drug bond in some antitumor active complexes of coinage metal ions. ACS Omega. 2020;5(42):26999–7015. https://doi.org/10.1021/acsomega.0c01471.

97. Mendizabal F, Burgos D, Olea-Azar C. Theoretical study of [Hg3 (o-C6F4) 3] η-{benzene}(n= 1, 2) complexes. Chem Phys Lett. 2008;463(1–3):272–7. https://doi.org/10.1016/j.cplett.2008.08.058.

98. Chakraborty P, Nag A, Paramasivam G, Natarajan G, Pradeep T. Fullerene-functionalized monolayer-protected silver clusters:[Ag$_{29}$(BDT)$_{12}$(C$_{60}$)$_n$]$^{3-}$ (n= 1–9). ACS Nano. 2018;12(3):2415–25. https://doi.org/10.1021/acsnano.7b07759.

99. Prajongtat P, Sriyab S, Zentgraf T, Hannongbua S. Optimisation of stability and charge transferability of ferrocene-encapsulated carbon nanotubes. Mol Phys. 2018;116(1):9–18. https://doi.org/10.1080/00268976.2017.1359348.

100. Johnson ER, DiLabio GA. Structure and binding energies in van der Waals dimers: comparison between density functional theory and correlated ab initio methods. Chem Phys Lett. 2006;419(4–6):333–9. https://doi.org/10.1016/j.cplett.2005.11.099.

101. Lawson-Daku LM, Vargas A, Hauser A, Fouqueau A, Casida ME. Assessment of density functionals for the high-spin/low-spin energy difference in the low-spin iron (ii) Tris (2,2′-bipyridine) complex. ChemPhysChem. 2005;6(7):1393–410. https://doi.org/10.1002/cphc.200400584.

102. Vargas A, Zerara M, Krausz E, Hauser A, Lawson-Daku LM. Density-functional theory investigation of the geometric, energetic, and optical properties of the cobalt (II) tris (2, 2′-bipyridine) complex in the high-spin and the jahn−teller active low-spin states. J Chem Theory Comput. 2006;2(5):1342–59. https://doi.org/10.1021/ct6001384.

103. Reed AE, Weinstock RB, Weinhold F. Natural population analysis. J Chem Phys. 1985;83(2):735–46. https://doi.org/10.1063/1.449486.

104. Hirshfeld FL. Bonded-atom fragments for describing molecular charge densities. Theor Chim Acta. 1977;44:129–38. https://doi.org/10.1007/BF00549096.

105. Wiberg KB, Rablen PR. Comparison of atomic charges derived via different procedures. J Comput Chem. 1993;14(12):1504–18. https://doi.org/10.1002/jcc.540141213.

Murcia-Galán *et al. BMC Chemistry*   (2023) 17:135

Page 21 of 21

106. Kosov DS, Popelier PLA. Atomic partitioning of molecular electrostatic potentials. J Phys Chem A. 2000;104(31):7339–45. https://doi.org/10.1021/jp0003407.

107. Andrada DM, Foroutan-Nejad C. Energy components in energy decomposition analysis (EDA) are path functions; why does it matter? Phys Chem Chem Phys. 2020;22(39):22459–64. https://doi.org/10.1039/d0cp04016a.

108. Morokuma K. Molecular orbital studies of hydrogen bonds. III. C═O···H-O hydrogen bond in H2CO··· H2O and H2CO··· 2H2O. J Chem Phys. 1971;55(3):1236–44. https://doi.org/10.1063/1.1676210.

109. Ziegler T, Rauk A. On the calculation of bonding energies by the Hartree Fock Slater method. Theor Chim Acta. 1977;46(1):1–10. https://doi.org/10.1007/BF00551648.

110. Kitaura K, Morokuma K. A new energy decomposition scheme for molecular interactions within the Hartree-Fock approximation. Int J Quantum Chem. 1976;10(2):325–40. https://doi.org/10.1002/qua.560100211.

111. Vyboishchikov SF, Krapp A, Frenking G. Two complementary molecular energy decomposition schemes: the Mayer and Ziegler-Rauk methods in comparison. J Chem Phys. 2008;129(14):144111. https://doi.org/10.1063/1.2989805.

112. Neese F, Wennmohs F, Becker U, Riplinger C. The ORCA quantum chemistry program package. J Chem Phys. 2020;152(22):224108. https://doi.org/10.1063/5.0004608.

113. Berendsen HJ, Postma JV, Van Gunsteren WF, DiNola ARHJ, Haak JR. Molecular dynamics with coupling to an external bath. J Chem Phys. 1984;81(8):3684–90. https://doi.org/10.1063/1.448118.

114. Martínez-Guajardo G, Cabellos JL, Díaz-Celaya A, Pan S, Islas R, Chattaraj PK, Heine T, Merino G. Dynamical behavior of borospherene: a nanobubble. Sci Rep. 2015;5(1):11287. https://doi.org/10.1038/srep11287.

Publisher's Note